SAPHARI

Safe and Autonomous Physical Human-Aware Robot Interaction

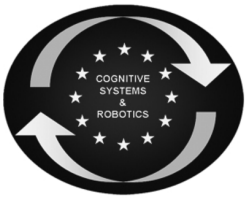

Project funded by the European Community's 7th Framework Programme (FP7-ICT-2011-7)
Grant Agreement ICT–287513

Deliverable D3.2.1

Control and estimation algorithms for VIA robots

Deliverable due date: 31 October 2013	**Actual submission date:** 31 December 2013
Start date of project: 1 November 2011	**Duration:** 48 months
Lead beneficiary: UNIROMA1	**Revision:** Final

Nature: R	**Dissemination level:** PU
R = Report P = Prototype D = Demonstrator O = Other	PU = Public PP = Restricted to other programme participants (including the Commission Services) RE = Restricted to a group specified by the consortium (including the Commission Services) CO = Confidential, only for members of the consortium (including the Commission Services)

Executive Summary

This deliverable of work package WP3 presents a summary of the most recent research results on estimation and control of robots with Variable Impedance Actuation (VIA) obtained by the partners of SAPHARI and developed during the first two years of the project.

The possibility of exploiting the characteristics of such devices in planning and feedback control requires the knowledge of the actual impedance of the robot joints. However, no sensor is available for the direct measure of such physical quantities. Therefore, in the first part of the document, three competitive approaches are presented for estimating the stiffness or damping of a single VIA joint. Emphasis is given to methods that are non-invasive (i.e., which can be used without modifying the device), require less sensing information, can work efficiently on line (so as to capture the time-varying nature of the problem), and are robust with respect to measurement or input noise and uncertainty in model parameters.

Experimental validation has been made on single-dof VSA and VDA units, but extension to multi-dof robots is rather straightforward, thanks to the decentralized design of the proposed methods. In the next period, we are planning to perform also a quantitative comparison of the performance of these estimation methods, which now constitute the state-of-the-art in the field, on the *qbmove* VSA systems developed within SAPHARI and recently distributed to the involved partners.

The second part of the document focuses on control laws that take advantage of the variable compliance (and nonlinear resonant modes) of the robot joints for generating desired cyclic motions. The underlying idea is to use the natural dynamics of VIA robots to induce, by means of a suitable attractive control action, a task-oriented periodic motion that is also very energy efficient. This can be used for highly dynamic and complex motions, such as hitting and throwing (with the robot upper body), or walking and running (with the lower limbs). Representative experimental results have been already obtained on the DLR Hand Arm System.

A final section is devoted to an optimal control problem for visco-elastic compliant joints, where analytical and numerical tools are used so as to achieve the largest possible link velocity in a given time. This is another example of the intensive research activity of SAPHARI on the optimization of dynamic performance of various classes of compliantly actuated robots, as already presented in milestone *MS3 Optimal control of modular VSA manipulators* reached @M12 and in the published scientific papers.

We also mention that activities within the specific task T3.2 of WP3 will continue as planned until the end of the project (the next deliverable *D3.2.2 Experimental validation of control laws for multi-dof VIA manipulators* is due @M48), so that the estimation and control results summarized in this document can be further developed, integrated, tested, and refined through practical use on different platforms.

Table of contents

1 Introduction

In this report we consider some estimation and control problems that arise in robots using Variable Impedance Actuation (VIA), and more specifically actuators that allow a variable stiffness (VSA) or variable physical damping (VDPA).

The need for estimating the actual stiffness and/or damping of such actuator/transmission units is due to the fact that there is no sensor available to measure directly these quantities. In turn, accurate values are needed for the best performance of model-based optimal/feedforward commands or for the implementation of advanced feedback laws, e.g., those guaranteeing simultaneous and decoupled motion-stiffness control.

The strong dynamic interplay between potential energy (due to transmission deflection) and kinetic energy in robots with constant or variable compliant joints poses new additional challenges beside the traditional control tasks of accurate trajectory tracking or stable force interaction. Suitable optimal control actions can be designed in order to obtain extremely large motion speeds and/or impulsive forces or, conversely, for preventing and excessive (unsafe) energy accumulation. It is also possible to exploit the natural vibrational dynamics of these nonlinear compliant mechanical systems to realize cyclic or periodic tasks in a robust and energy-efficient way.

After recalling in Sec.2 the basic dynamic modeling for robotic devices with VSA, the two Sections 3 and 4 present the latest and most robust versions of the stiffness estimation algorithms developed by UNIPI and UNIROMA1, respectively, for a single-dof antagonistic VSA unit. Both approaches work on the motor side of the compliant transmission units, and can thus be immediately generalized to the multi-dof case. Moreover, they do not require necessarily a joint torque sensor. They differ in the processing of measured data, which is done in order to avoid differentiation of noisy measures, in the way measurements are filtered, and in the actual implementation of the following Recursive Least Squares (RLS) method.

Section 5 presents the extension by IIT of a similar approach for the estimation of damping in a VDPA. Special care is used to address the time-varying nature of frictional phenomena (e.g., in the used clutch).

Two control approaches for generating cyclic motions in compliant robots are proposed by DLR in Sect. 6. The first method exactly decouples the partially feedback linearized dynamics of the robot using complete model information, and yields then a globally attractive limit cycle along a desired oscillation mode. The second method directly excites the natural dominant oscillation mode of the compliant robot, requiring no model knowledge but only measurements of the states of the actuated joints.

Finally, the short Section 7 is devoted to an optimal control problem in which the role of damping is investigated, when trying to maximize in a finite time window the velocity of a link driven by a visco-elastic joint. This result by DLR complements the previous activities of this partner and of UNIPI on the use of optimal control tools and methods for optimizing the dynamic performance of VIA-based robots.

2 Dynamic modeling

Flexible transmissions are characterized by elastic elements that allow a deformation (or displacement) ϕ between the motor angle θ and the link angle q ($\phi = q - \theta$). A smooth potential function $U_e(\phi) \geq 0$ is associated to the deformation ϕ, with $U_e(\phi) = 0$ iff $\phi = 0$. The flexibility torque across the transmission is $\tau_e(\phi) = \partial U_e(\phi)/\partial\phi$. The stiffness of the transmission is defined as the variation rate of the flexibility torque $\tau_e(\phi)$ w.r.t. the deformation ϕ,

$$\sigma(\phi) = \frac{\partial \tau_e(\phi)}{\partial q} = \frac{\partial \tau_e(\phi)}{\partial \phi} > 0. \tag{1}$$

For a single motor driving a rigid link subject to gravity through a (nonlinear) flexible transmission, see

Fig. 1(a), the dynamic model takes the form

$$M\ddot{q} + D_q\dot{q} + \tau_e(\phi) + g(q) = \tau_{\text{ext}} \tag{2}$$

$$B\ddot{\theta} + D_\theta\dot{\theta} - \tau_e(\phi) = \tau, \tag{3}$$

where $M > 0$ and $B > 0$ are the link and motor inertias, $D_q \geq 0$ and $D_\theta \geq 0$ are the viscous friction coefficients at the two sides of the transmission, τ is the control torque on the motor side, and $g(q)$ and τ_{ext} are respectively the gravity and the environment/disturbance torques acting on the link.

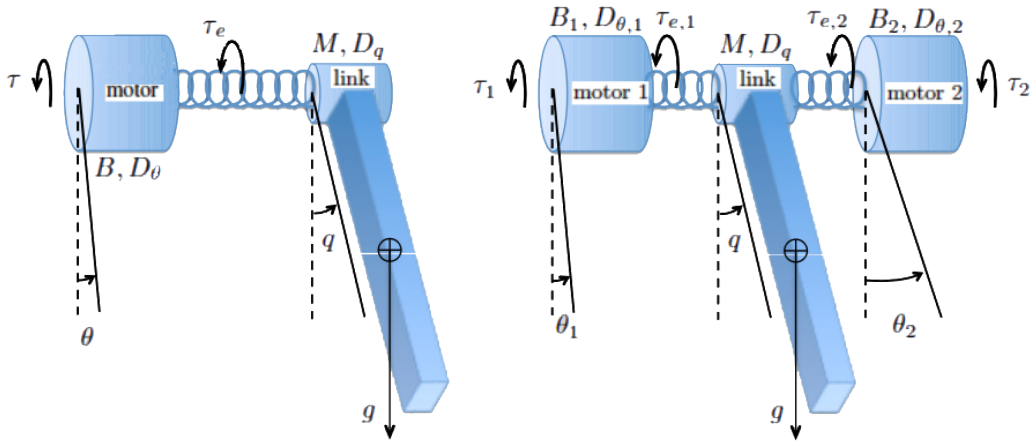

(a) (b)

Figure 1: Schematic models of a link driven (a) by a single flexible transmission, or (b) by a VSA in antagonistic arrangement

An antagonistic Variable Stiffness Actuator (VSA), see Fig. 1(b), is characterized by two motors working in parallel and antagonistically connected to the driven link through nonlinear transmissions. Although different arrangements are possible, we will consider here only the bi-directional one, which is also denoted as the Agonistic-Antagonistic (AA) configuration, see [2]. Depending on the realization, the nonlinearity of the deformation/torque characteristic of the transmissions results either by the use of nonlinear (e.g., cubic or exponential) springs or by the arrangement of linear springs in a nonlinear kinematic mechanism. Representative devices in this class are the biologically inspired VSA [31] and the VSA-II [41].

The pair of motor-transmission units are modeled with two similar equations of the form (3), where each motor-transmission undergoes a deformation $\phi_i = q - \theta_i$, for $i = 1, 2$. The dynamics of an antagonistic VSA is thus

$$M\ddot{q} + D_q\dot{q} + \tau_{e,t}(\boldsymbol{\phi}) + g(q) = \tau_{\text{ext}} \tag{4}$$

$$B_{\theta,i}\ddot{\theta}_i + D_{\theta,i}\dot{\theta}_i - \tau_{e,i}(\phi_i) = \tau_i, \quad i = 1, 2. \tag{5}$$

In this case, the *(total) flexibility torque* transmitted to the driven link and the associated *(total) device stiffness* are given respectively by

$$\tau_{e,t} = \tau_{e,1}(\phi_1) + \tau_{e,2}(\phi_2) \tag{6}$$

and

$$\sigma_t(\boldsymbol{\phi}) = \sigma_1(\phi_1) + \sigma_2(\phi_2), \tag{7}$$

where

$$\sigma_i(\phi_i) = \frac{\partial \tau_{e,i}(\phi_i)}{\partial \phi_i} > 0, \quad i = 1, 2, \tag{8}$$

are the local stiffnesses of the two transmissions and $\boldsymbol{\phi} = (\phi_1 \ \phi_2)^T$. We stress the separability of the functions (6) and (7), whereas one has in general $\phi_1 \neq \phi_2$. Most of the times the two motor-transmission units are identical (perfect symmetry). However, our later developments apply directly also to the general case.

A general dynamic model of a n-dof manipulator driven by VSA can be written by compounding the robot link dynamics with the proper m motor equations.

For multi-dof robots using VSA in antagonistic configurations, we have $m = 2n$ and the motor equations are of the form (5) introduced above. For serial configurations of VSA (like in the case of the DLR VS joint or the IIT AwAS device), we still have $m = 2n$ motors, but the two motors at each joint are different in size, functionality, and mathematical model. Sometimes, the assumption is made that the dynamics of the smaller motors used to adjust the joint stiffness can be neglected. In that case, only $m = n$ differential equations are left in the dynamic model describing the principal motors that actuate the n robot links through (nonlinear) flexible transmissions, while another vector of $m = n$ static parameters is present that can be instantaneously changed in order to modify the robot joint stiffnesses. With this in mind, we will let the number m of motor equations unspecified so as to cover all interesting situations.

Furthermore, we take a similar assumption as in the modeling robots with elastic joints of constant stiffness [44], namely that the rotational kinetic energy of the rotors of the two motors at each joint is due only to their own spinning. Under this assumption, and neglecting for simplicity dissipative terms, the dynamic model for a multi-link robot driven by (serial or antagonistic) VSA takes the form

$$\boldsymbol{M}(\boldsymbol{q})\ddot{\boldsymbol{q}} + \boldsymbol{C}(\boldsymbol{q}, \dot{\boldsymbol{q}})\dot{\boldsymbol{q}} + \boldsymbol{g}(\boldsymbol{q}) = \boldsymbol{\tau}_e \tag{9}$$

$$\boldsymbol{B}\ddot{\boldsymbol{\theta}} + \boldsymbol{\tau}_e = \boldsymbol{\tau} \tag{10}$$

$$\boldsymbol{\tau}_e = \left(\frac{\partial U_e(\boldsymbol{\theta}, \boldsymbol{q}, \boldsymbol{\pi}_{\boldsymbol{\sigma}})}{\partial \boldsymbol{\theta}} \right)^T = \boldsymbol{\psi}(\boldsymbol{\theta} - \boldsymbol{q}, \boldsymbol{\pi}_{\boldsymbol{\sigma}}), \tag{11}$$

where $\boldsymbol{M}(\boldsymbol{q}) \in \mathbb{R}^{n \times n}$ is the symmetric and positive definite link inertia matrix, $\boldsymbol{C}(\boldsymbol{q}, \dot{\boldsymbol{q}})\dot{\boldsymbol{q}}$ are the Coriolis/centrifugal terms, $\boldsymbol{g}(\boldsymbol{q})$ is the gravitational term, and $\boldsymbol{B} \in \mathbb{R}^{m \times m}$ denotes the constant, diagonal, and positive definite motor inertia matrix. Moreover, $\boldsymbol{\pi}_{\boldsymbol{\sigma}} \in \mathbb{R}^m$ is a set of parameters possibly used to change the stiffness characteristics of the flexible transmissions. The robot configuration variables $\boldsymbol{x} = (\boldsymbol{\theta}^T \ \boldsymbol{q}^T)^T \in \mathbb{R}^{m+n}$ can be divided into motor positions $\boldsymbol{\theta} \in \mathbb{R}^m$ and link positions $\boldsymbol{q} \in \mathbb{R}^n$. Only the motor states $(\boldsymbol{\theta}, \dot{\boldsymbol{\theta}})$ are directly actuated via the control input $\boldsymbol{\tau} \in \mathbb{R}^m$. In most cases, including the DLR Hand-Arm VSA-based system, the vector function $\boldsymbol{\psi}$ that expresses the flexibility torques across the flexible transmissions has a local, separable dependence: for the generic joint i, we have $\psi_i = \psi_(\theta_i - q_i)$ (the parametric dependence on π_{σ_i} is often dropped). Note that the definition of the flexibility torque in eq. (11) has the opposite sign with respect to the one used in eqs. (2–3) or (4–5). In Sect. 6 on control, we will also use the property that the inverse function $\boldsymbol{\psi}^{-1}$ exists, and thus that $\boldsymbol{\theta} - \boldsymbol{q} = \boldsymbol{\psi}^{-1}(\boldsymbol{\tau}_e)$.

3 Stiffness estimation using modulating functions

We consider the problem of estimating the nonlinear stiffness of a single VSA in Agonistic-Antagonist (AA) configuration. We propose here an algorithm based on modulating functions. which allow to avoid the need of numerical derivatives and for which the tuning is very simple. An analysis of the errors indicates the nature of the estimation convergence and provides guidelines for tuning the parameters of the algorithm.

We first present the modulating functions and give some useful properties that are used then to define the stiffness estimator. The effects of measurement noise and truncation errors are analyzed next. Simulation results are provided to illustrate the role of parameters of the algorithm on performance, and finally the method is validated on experimental data. The results summarized in this section are presented in [29] and in the submitted paper [30].

3.1 Modulating functions

The following definitions and proposition come from [37], and have been slightly modified for our needs.

Definition 1 *A modulating function of order h on $[a,b]$ ($a,b \in \mathbb{R}$) is a function $\psi : [a,b] \to \mathbb{R}$, h-times differentiable such that:*

$$d^i\psi(a) = d^i\psi(b) = 0, \quad i = 0,\dots,h-1, \tag{12}$$

where d^i represent the i-th order derivative.

Example 1 *Let us define the following function:*

$$w_{i,j}(u) = (1-u)^i u^j, \quad u \in \mathbb{R},\ i,j \in \mathbb{N}. \tag{13}$$

Then, $w_{h,h}$, for $h \in \mathbb{N}$, is a modulating function of order $h+1$ on $[0,1]$.

Definition 2 *A function $f : [a,b] \to \mathbb{R}$ integrable on $[a,b]$ is modulated by taking the inner product with a modulating function ψ:*

$$\langle f, \psi \rangle = \int_a^b f(u)\psi(u)du. \tag{14}$$

Proposition 1 *Let f_1, f_2 be integrable real valued functions on $[a,b]$, ψ a modulating function of order h on $[a,b]$ and $C \in \mathbb{R}$ a constant. Then, we have the following properties:*

1. $\langle d^i f_1, \psi \rangle = (-1)^i \langle f_1, d^i\psi \rangle, \quad i = 0,\dots,k-1,$
2. $\langle C f_1 + f_2, \psi \rangle = C\langle f_1, \psi \rangle + \langle f_2, \psi \rangle.$

Property 1 is very important, because it allows to replace a derivative of a function f, which is usually unknown or uncertain (for example, we only have access to a measured signal), by the derivative of the modulating function for which the derivative is known and can be computed analytically.

3.2 Estimation algorithm

The estimation of the stiffness is derived from the two equations (5), that is, we look at the system on the motor side. The algorithm is split into two parts. In the first part, the equations are differentiated to make the stiffness appear explicitly, the stiffness is approximated by a Taylor expansion, and the resulting equations are transformed, using modulating functions, so that only filtered versions of the measured signals are needed. In the second part, a Recurslve Least Squares (RLS) algorithm is used to estimate the coefficients of the Taylor expansion, and thus the stiffness itself.

We start from equation (5), that is:

$$\tau_{e,i}(\phi_i) = B_i\ddot{\theta}_i + D_{\theta,i}\dot{\theta}_i - \tau_i, \qquad i = 1,2. \tag{15}$$

Differentiating with respect to time the motor equations yields

$$\phi_i^{(1)}\sigma_i(\phi) = B_i\theta_i^{(3)} + D_{\theta,i}\theta_i^{(2)} - \tau_i^{(1)}, \tag{16}$$

where the shorthand notation $x^{(i)}$ has been used to denote the i-th derivative of a variable x w.r.t. time. We take the following Taylor expansion approximation of order N (i.e., with $N+1$ coefficients)

$$\sigma_i(\phi_i) \approx \sum_{j=0}^{N} \alpha_j^i \frac{(\phi_i)^j}{j!}, \tag{17}$$

which gives the relation

$$\sum_{j=0}^{N} \alpha_j^i \frac{\phi_i^{(1)}(\phi_i)^j}{j!} = B_i\theta_i^{(3)} + D_{\theta,i}\theta_i^{(2)} - \tau_i^{(1)}. \tag{18}$$

Since the maximum derivative order is three, we need to take a modulating function ψ of order $h = 4$, which will be defined later. Modulating eq. (18) with ψ, one obtains by Proposition 1:

$$\left\langle \sum_{j=0}^{N} \alpha_j^i \frac{\phi_i^{(1)}(\phi_i)^j}{j!}, \psi \right\rangle = \left\langle B_i\theta_i^{(3)} + D_{\theta,i}\theta_i^{(2)} - \tau_{e,i}^{(1)}, \psi \right\rangle, \tag{19}$$

$$\sum_{j=0}^{N} \alpha_j^i \left\langle d\left(\frac{(\phi_i)^{j+1}}{(j+1)!}\right), \psi \right\rangle = B_i \left\langle d^3\theta_i, \psi \right\rangle + D_{\theta,i} \left\langle d^2\theta_i, \psi \right\rangle - \left\langle d\tau_{e,i}, \psi \right\rangle, \tag{20}$$

$$\sum_{j=0}^{N} \alpha_j^i \left\langle \frac{(\phi_i)^{j+1}}{(j+1)!}, d\psi \right\rangle = B_i \left\langle \theta_i, d^3\psi \right\rangle - D_{\theta,i} \left\langle \theta_i, d^2\psi \right\rangle - \left\langle \tau_{e,i}, d\psi \right\rangle. \tag{21}$$

Therefore, the above is a relation between the stiffness and the measured signals θ_i and $\tau_{e,i}$, where the only source of error is in the Taylor approximation of the σ_i, $i = 1, 2$.

If we want to estimate the parameters α_i with a RLS algorithm, then we need a relation that shifts with time t. For this purpose, we consider $a = t - T$ and $b = t$ for the domain of the modulating function ψ, T being the length of the integration window. Then, the modulating function is taken as $\psi(u) = (u - t + T)^3(t - u)^3$. We have the following relation:

$$\begin{aligned}\sum_{j=0}^{N} \alpha_j^i \int_{t-T}^{t} \frac{(\phi_i)^{j+1}}{(j+1)!}(u)\,(d\psi)\,(u)du = {} & B_i \int_{t-T}^{t} \theta_i(u)\left(d^3\psi\right)(u)du - D_{\theta,i}\int_{t-T}^{t} \theta_i(u)\left(d^2\psi\right)(u)du \\ & - \int_{t-T}^{t} \tau_{e,i}(u)\,(d\psi)\,(u)du.\end{aligned} \tag{22}$$

Performing the change of variable $u = T\nu + t - T$ and dividing by T^3 yields

$$\begin{aligned}\sum_{j=0}^{N} \alpha_j^i \left(T^2 \int_0^1 \frac{(\phi_i)^{j+1}}{(j+1)!}(t + T(\nu-1))(dw_{3,3})(\nu)d\nu\right) = {} & B_i \int_0^1 \theta_i(t + T(\nu-1))(d^3w_{3,3})(\nu)d\nu \\ & - D_{\theta,i}T\int_0^1 \theta_i(t + T(\nu-1))(d^2w_{3,3})(\nu)d\nu \\ & - T^2\int_0^1 \tau_{e,i}(t + T(\nu-1))(dw_{3,3})(\nu)d\nu,\end{aligned} \tag{23}$$

where the function $w_{3,3}$ is one of those defined by eq. (13), namely for equal $h = 3$.

In order to obtain a discrete-time version of this relation, we assume that the sampling period is T_s and that the integration window is a multiple of this period, $T = HT_s$, with $H \in \mathbb{N}$. Then, we take an approximation of the integral with the trapezoidal method, that is:

$$\int_0^1 f(u)du \approx \sum_{m=0}^{H} W_m f(t_m), \tag{24}$$

with $t_m = mT_s$, $W_0 = W_M = T_s/2$ and $W_m = T_s$, $m = 1, \ldots, H-1$.

We finally obtain the following relation at the discrete-time sample k (corresponding to the continuous time $t = kT_s$):

$$\boldsymbol{C}_i(k) = \sum_{j=0}^{N} \alpha_j^i \gamma_j^i(k) \triangleq \boldsymbol{A}_i^T \boldsymbol{\Gamma}(k), \tag{25}$$

with $\boldsymbol{A}_i = [\alpha_0^i, \ldots, \alpha_N^i]^T$, $\boldsymbol{\Gamma}(k) = [\gamma_0^i, \ldots \gamma_N^i]^T$, and where

$$\begin{aligned}\boldsymbol{C}_i(k) \;=\; & \sum_{m=0}^{H} \theta_i\left((k-m)T_s\right) \times \left(B_i W_m (d^3 w_{3,3})(m/H) - D_{\theta,i} W_m T (d^2 w_{3,3})(m/M)\right) \\ & + \sum_{m=0}^{H} \tau_{e,i}\left((k-m)T_s\right)\left(-T^2 W_m (d w_{3,3})(m/M)\right)\end{aligned} \tag{26}$$

and

$$\gamma_j^i(k) = \sum_{m=0}^{H} \left(\frac{\phi_i^{j+1}}{(j+1)!}\right)\left((k-m)T_s\right)\left(T^2 W_m (d w_{3,3})(m/H)\right). \tag{27}$$

For $k \leq H$, measured values at negative instants of times $(k-m)T_s$, i.e., with $k-m<0$, are simply set to zero. The derivatives of $w_{3,3}$ needed in eq. (26) are given by:

$$d w_{3,3}(u) \;=\; -3w_{2,3} + 3w_{3,2}, \tag{28}$$

$$d^2 w_{3,3}(u) \;=\; 6w_{1,3}(u) - 18w_{2,2}(u) + 6w_{3,1}(u), \tag{29}$$

$$d^3 w_{3,3}(u) \;=\; 6w_{0,3}(u) + 54w_{1,2}(u) - 54w_{2,1}(u) + 6w_{3,0}(u). \tag{30}$$

Note that the definition of $\boldsymbol{\Gamma}_i$ and $\boldsymbol{C}_i$ can be seen as filtering by a *Finite Impulse Response* (FIR) digital filter. With the obtained discrete-time relation (25) between the stiffness parameters in the Taylor expansion and the measured signals, we can use a standard RLS algorithm (see, e.g., [27]) in order to obtain an approximation $\hat{\boldsymbol{A}}_i$ of $\boldsymbol{A}_i$.

3.3 Error analysis and robustness

The estimation method just presented is made essentially of two steps: first, a relation between filtered versions of the measured data and the coefficients of the Taylor expansion of the stiffness is derived, then it is used in a least squares algorithm. In principle, assuming perfect motor data, three are the possible sources of errors: noise on the measurements (and on the actuating torques), truncation in the Taylor expansion, and numerical integration errors. The noise ω added to the measured data is assumed to be a stochastic variable with zero mean and finite variance. On the other hand, the numerical integration error is assumed to be negligible. Reduction of the estimation error is pursued here by a suitable choice of parameters made only within the first step of the method: we will see how to set design parameters so as to reduce sufficiently the negative effects on the second step of the method. In particular, we shall treat analytically only the noise on the actuating torques τ_i ($i = 1.2$). Position sensors are fairly accurate, and so the effect of a small noise on position measurements will be considered only in simulations.

Taking errors into account, equation (25) can be rewritten as follows:

$$\boldsymbol{A}_i^T \boldsymbol{\Gamma}(k) = \boldsymbol{C}_i(k) + e_{R_N}^i(k) + e_\omega^i(k), \qquad i = 1, 2, \tag{31}$$

where $e_{R_n}^i(k)$ is the error due to truncation and $e_\omega^i(k)$ is the error due to noise (index i is for the two transmissions of the VSA). Three different parameters can be used to reduce these errors: the length of the integration window T, the order of the Taylor expansion M, and the sampling period T_s (note that these parameters are linked via the relation $H = T/T_s$).

Analysis of $e^i_{R_N}$ We start from equation (18), replacing the approximation of the stiffness by its true expression and following the same computations made for the proposed estimation method. We obtain:

$$e^i_{R_N}(k) = \sum_{m=0}^{H} (\sigma_i - \sigma_i^{N+1}) \cdot (\phi_i)((k-m)T_s) \cdot T^2 \cdot W_m(dw_{3,3}(m/M)), \tag{32}$$

where σ_i^{N+1} is the Taylor expansion of σ_i up to order $N+1$. From the expression of the truncation error, we see that in order to get a bound on this error, the transmission deformation ϕ_i has to be bounded. Hence, we assume that there exist $\varepsilon_1^i, \varepsilon_2^i$ such that $\phi_i(k) \in [\varepsilon_1^i, \varepsilon_2^i]$ for all $k \geq 0$. Applying then Proposition 2 in [26], one has

$$|e^i_{R_N}(k)| \leq T \cdot \frac{5}{8} \sup_{\phi_i \in [\varepsilon_1^i, \varepsilon_2^i]} |\sigma_i(\phi_i) - \sigma_i^{N+1}(\phi_i)|, \qquad i = 1, 2. \tag{33}$$

Analysis of e^i_ω We assume here that ω is a white noise with zero mean and finite variance. Similarly to the truncation error, we obtain that the noise error contribution is equal to

$$e^i_\omega(k) = \sum_{m=0}^{H} \omega((k-m)T_s) T^2 W_m(dw_{3,3}(m/M)), \qquad i = 1, 2. \tag{34}$$

Applying Corollary 2 in [26], it follows that $e_\omega(k)$ converges to zero as H goes to infinity.

Setting of parameters The effect of the parameters on the different errors is summarized in Tab. 1. From the previous analysis, we can derive some indications for the tuning of the parameters. First, the sampling period T_s should be taken as small as possible in order to reduce the effect of the noise. The length of the integration window should be taken large enough to filter the noise, depending on the relative power between signal and noise, which itself depends on the type and quality of the sensors. Even if increasing T will increase the truncation error, we see from eq, (33) that this relation is linear, and typical values of T belong to the interval $[0.1, 2]$ s. The setting of T and N can be done independently, and the latter value will highly depend on the range of transmission deformations ϕ_i.

	Truncation error	Noise error contribution
$N \uparrow$	$\searrow$	$\longleftrightarrow$
$T_s \uparrow$	$\longleftrightarrow$	$\searrow$
$T \uparrow$	$\nearrow$	$\searrow$

Table 1: Effect of parameters on the different types of errors

Convergence of the RLS We have shown until now that the error contributions can be made arbitrarily small, uniformly with respect to time, by suitable tuning of some parameters in the method. The effect of uniformly bounded errors on the estimation with a standard RLS algorithm have been studied in [13]. From Theorem 1 therein we obtain that, for uniformly bounded noise, the estimation error on the coefficients of the Taylor expansion goes to zero as the bound on the error goes to zero. Thus, the error on the Taylor coefficients (and hence the error on the stiffness itself) will eventually converge to zero. The conclusion is that we can achieve arbitrarily small estimation errors on the stiffness by suitable tuning the design parameters of the method.

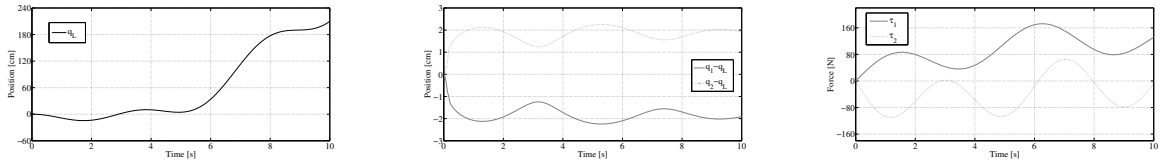

(a) link position (b) clean deformations (c) clean input torques

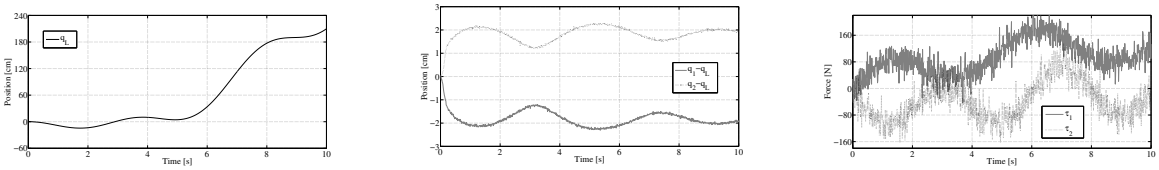

(d) link position (e) noisy deformations (f) noisy input torques

Figure 2: Clean (top) and noisy (bottom) data signals used in the simulations (deformations $\phi_i = q - \theta_i$ are affected by noise introduced on the measured motor positions θ_i, for $i = 1, 2$)

3.4 Simulation results

We have considered an Agonistic-Antagonist VSA mechanism realized with two identical cubic springs whose torque-deformation characteristic is described by the flexibility torque expression:

$$\tau_{e,i} = 10(q - \theta_i)^3, \qquad i = 1, 2. \tag{35}$$

The motor and link parameters in eqs. (4–5) are: $B_1 = B_2 = 10^{-4}$ [kg m^{-2}], $M = 0.0179$ [kg m^{-2}], $D_{\theta,1} = D_{\theta,2} = 1.27$ [Nm s/rad], and $D_q = 0.0127$ [Nm s/rad]. We consider only the case without gravity, i.e., $g = 0$.

We provide here the results of representative simulations using the the proposed method. The estimation method was run on the sets of measurement data reported in Fig. 2. In order to precisely evaluate the effects of noise on the reconstruction of the device stiffness, three different cases are compared in simulation: without noise, with white noise affecting the input torques τ_i only, and finally with white noise affecting both the input torques and the motor positions θ_i (and thus, the deformations $\phi_i = q - \theta_i$ that enter in the computations). The measurement of the link position q is assumed to be ideal.

The importance of noise is quantified by the Signal-to-Noise Ratio:

$$SNR = 20 \log_{10} \frac{Var(signal\ without\ noise)}{Var(noise)}.$$

Tthe lower is the SNR, the more significant is the noise. Noise on the flexibility torque measurements has been taken large, corresponding to $SNR = 9$, while noise on motor positions was low with a $SNR = 140$. We have also compared the effect of N in eq. (17) on the stiffness estimation. The best value in this case would be $N = 2$, because the assumed flexibility torques are cubic polynomials in ϕ_i and thus the stiffness is a quadratic function. Since the actual behavior of the springs in the transmissions might not be strictly polynomial (e.g., we may consider also exponential springs), we have tested our algorithm both with $N = 2$ and $N = 4$ (which means, respectively, three and five coefficients in the Taylor expansion (17)).

The other design parameters are set as follow: the length of the integration window is $T = 0.5$ s, the sampling time is taken as $T_s = 0.001$ s, while the covariance matrix for the RLS is initialized at $\boldsymbol{P}(0) = 10^8 \cdot \boldsymbol{I}_{N+1}$. The stiffness estimation results are given in Fig. 3. These are also summarized in Tab. 2, where the average of the Mean Square Error (MSE) and Mean Square Relative Error Percentage (MSREP), see, e.g., [9], have been

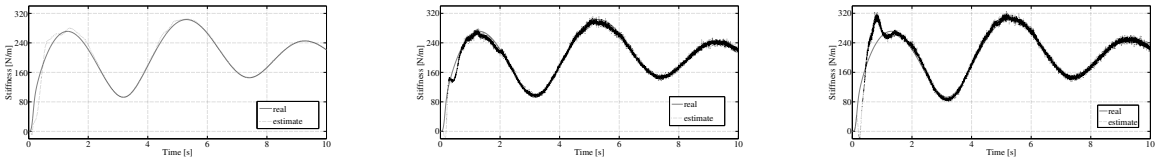

(a) Noisy torques and clean positions, with $N = 2$ (b) Noisy torques and positions, with $N = 2$ (c) Noisy torques and positions, with $N = 4$

Figure 3: Stiffness estimation results with different combinations of clean and noisy signals and with different order of the Taylor expansion

computed over 100 simulations. Both MSE and MSREP were evaluated using only data after convergence of the estimation process converged, that is between $t = 2$ s and $t = 10$ s. We can see that in every case and with the same settings, the method performs satisfactorily.

	operative conditions	MSE	MSREP
$N = 2$	no noise	$3.4\,10^{-2}$	$5\,10^{-5}$
$N = 2$	noise on torques	19.3	$4.8\,10^{-2}$
$N = 2$	noise on torques and positions	38.4	$1\,10^{-1}$
$N = 4$	noise on torques	39.9	$8.7\,10^{-2}$
$N = 4$	noise on torques and positions	56.7	$1.2\,10^{-1}$

Table 2: Statistical evaluation of simulation results

3.5 Experimental results

We have tested the method on the Agonistic-Antagonistic VSA experimental device with exponential springs shown in Fig. 4 and fully described in [12].

In the experiments, the order of the Taylor expansion was set to $N = 9$ and the length of the integration window was $T = 0.5$ s. The initialization of the covariance matrix for the RLS algorithm was set to $\boldsymbol{P}(0) = 10^5 \cdot \Im_{10}$. The results of the stiffness estimation are shown in Fig. 5. We used a nominal model for comparison, although this not exact due to uncertainties in the parameters of the actuator. Therefore, we consider that the acquired knowledge of the stiffness is reliable up to an error about 25 %, represented by the horizontal line in Fig. 5b).

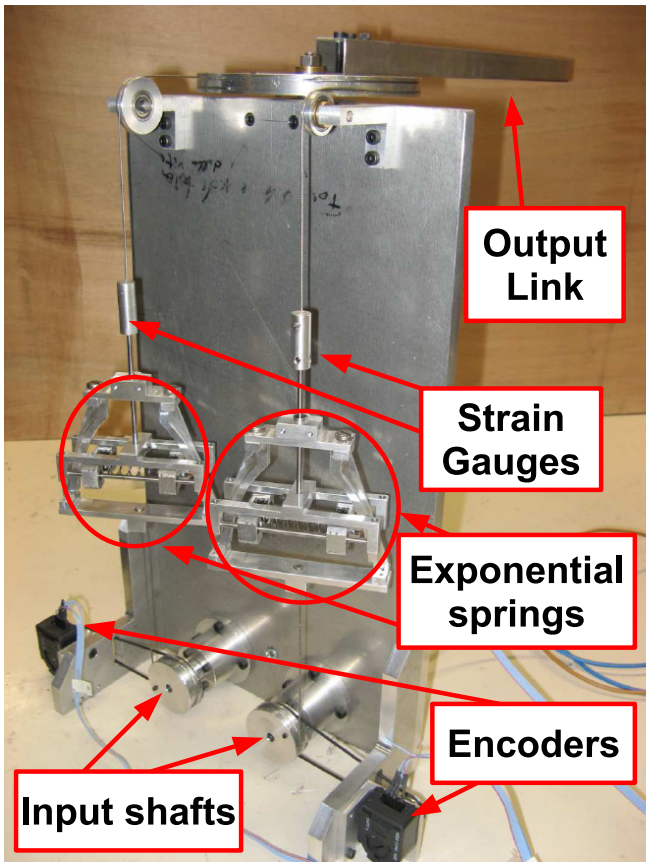

(a) experimental setup

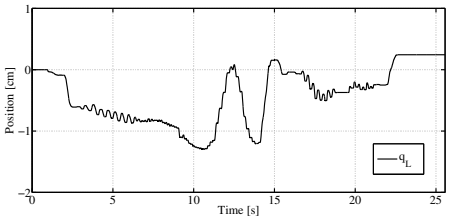

(b) link position

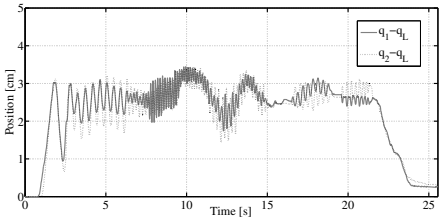

(c) deformations

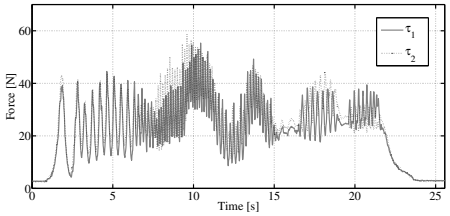

(d) flexibility torques

Figure 4: The experimental setup on the left consists of an antagonistic VSA system with exponential springs, realized using a linear spring forced to move on a suitable cam profile. Force sensors (strain gauges) are mounted on the tendons connecting the springs to the link. Position sensors (encoders) are mounted on the link and on two tendon pulleys coupled to the input levers. The collected experimental data measurements are shown on the right: link position, deformations, and flexibility torques

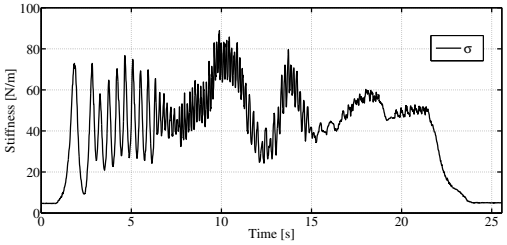

(a) total device stiffness

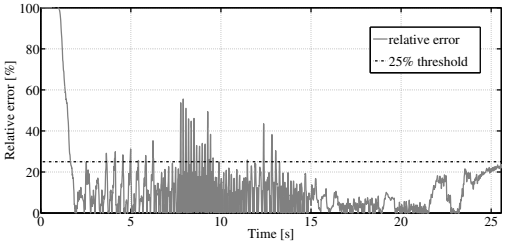

(b) relative error

Figure 5: Experimental stiffness estimation (a) for the VSA of Fig. 4 and its relative error (b) w.r.t. a nominal model

4 Signal-based stiffness estimation

We present next a stiffness estimation method in VSA-based systems that builds upon the residual approach presented in [9]. A main feature of that approach was its applicability with or without the use of a joint torque sensor. In addition, the method presented here does not use any knowledge about model parameters (i.e., we relax also the need of knowing the inertia and damping of the motors). Therefore, the method is purely based on input and output measurable signals. The results summarized in this section are detailed in the submitted paper [8].

As done already in Sec. 3 and in [9], we shall work on the motor side of an antagonistic VSA, where we can estimate the stiffness of each transmission separately, and then compute the total stiffness of the device using eq. (7). Therefore, we shall drop in the following the index $i = 1, 2$ in eq. (5), since the treatment is parallel but identical for the two transmissions. Equivalently, we can just consider the motor equation (3)

Integrating in time the motor equation gives

$$B\dot{\theta} + D_\theta \theta - \int_0^t \tau_e(\phi) ds = \int_0^t \tau ds. \tag{36}$$

This representation removes the presence of the second time derivative of the motor position output, which is difficult to numerically estimate in the presence of sensor noise. At this stage, the flexibility torque $\tau_e(\phi)$ can be approximated by using a linear combination of m polynomial basis functions $f_i(\phi)$, $i = 1 \dots m$:

$$\tau_e(\phi) \approx \sum_{i=1}^{m} \alpha_i f_i(\phi). \tag{37}$$

We note that eq. (37) plays a similar role as eq. (17) in Sect. 3. Indeed, the two approximations are defined on different, but differentially related quantities: the flexibility torque here, and the stiffness in the previous section. On the other hand, the N-th order Taylor expansion is a particular case of (37), when $f_i(\phi) = \phi^{i-1}$ and $m = N + 1$. However, the present approximation is more flexible than the Taylor expansion, since we can enforce a priori some desired structure to the solution. A typical example is when the flexibility torque is known to behave in a skew-symmetric way around $\phi = 0$, i.e., $\tau_e(-\phi) = -\tau_e(\phi)$. Then, only odd powers of i will be considered, $f_i(\phi) = \phi^{2i-1}$, with a saving on the total number of coefficients.

We can rewrite now eq. (36) as

$$B\dot{\theta} + D_\theta \theta - \sum_{i}^{m} \alpha_i \int_0^t f_i(\phi) ds = \int_0^t \tau ds. \tag{38}$$

Assuming that only the input and output signals (τ, θ, ϕ, and $\dot{\theta}$) are known, we have to estimate the parameter vector $\boldsymbol{\alpha} = (\alpha_1 \quad \alpha_2 \quad \dots \quad \alpha_m)$ of the function fitting the flexible torque in (37), as well as the motor inertia B and damping D_θ. Thus, we would like to find the parameter vector $\boldsymbol{\xi} = (B \quad D_\theta \quad \boldsymbol{\alpha})$ of dimension $n = (m + 2)$ that minimizes the square of the residual error

$$\left(\int_0^t \tau ds - \boldsymbol{F}^T \boldsymbol{\xi} \right)^2, \tag{39}$$

where

$$\boldsymbol{F}^T = \left(\dot{\theta} \quad \theta \quad \int_0^t f_1(\phi) ds \quad \dots \quad \int_0^t f_m(\phi) ds \right).$$

In a discrete-time approach with T_s as the sampling time, we can consider a data set composed by a matrix $\boldsymbol{A}$ that contains l vectors $\boldsymbol{F}_k = \boldsymbol{F}(t_k)$, sampled at $t = t_k = kT_s$,

$$\boldsymbol{A} = \left(\begin{array}{cccc} \boldsymbol{F}_1 & \boldsymbol{F}_2 & \dots & \boldsymbol{F}_l \end{array} \right)^T, \tag{40}$$

and by the vector

$$\boldsymbol{b} = \left(\int_0^{t_1} \tau ds \quad \int_0^{t_2} \tau ds \quad \dots \quad \int_0^{t_l} \tau ds \right)^T. \tag{41}$$

The parameter vector estimate that provides the least square error (39) in a *batch mode*, namely considering the whole data set, is obtained by pseudo-inversion of matrix $\boldsymbol{A}$:

$$\hat{\boldsymbol{\xi}} = \boldsymbol{A}^{\#} \boldsymbol{b}. \tag{42}$$

From the estimated parameter vector $\hat{\boldsymbol{\xi}}$, we extract directly the estimated motor inertia $\hat{B}$ and motor damping $\hat{D}_\theta$. The estimated stiffness is obtained as

$$\hat{\sigma} = \sum_i^m \hat{\alpha}_i \frac{\partial f_i(\phi)}{\partial \phi} = \sum_i^m \hat{\alpha}_i g_i(\phi). \tag{43}$$

Note that the functions $g_i(\phi)$ are available analytically.

4.1 On-line robust implementation

The approach represented by eqs. (40–42) collects a batch of data and is evaluated offline: therefore, it assumes that the parameter vector $\boldsymbol{\xi}$ is constant over time. This assumption is not general enough. The motor inertia B and damping D_θ can be assumed constant during an experiment, although they still need to be identified from time to time, and this generally requires disassembling the joint and disconnecting the flexible transmissions. On the other hand, the parameter vector $\boldsymbol{\alpha}$ cannot be considered constant during an experiment, mainly for two reasons: i) the transmission characteristics slightly changes over time, due to variation of temperature and stress caused by repetitive movements; ii) the approximation (37) may not able to capture well the flexibility torque characteristics in all its domain (except for simple or ad-hoc transmissions), and thus the parameter $\boldsymbol{\alpha}$ has to be slowly adapted when changing the working point of the device.

The use of a Recursive Least Squares (RLS) algorithm for on-line estimatation of the stiffness in a VSA device was originally proposed in [6], and then used also in [7,9,29] as well as by the method presented in the previous section. The principal drawback of the RLS algorithm is its sensitivity to poor excitation conditions. In such cases, the estimation of the inverse correlation matrix $(\boldsymbol{A}^T\boldsymbol{A})^{-1}$ loses the property of positive definiteness and/or symmetry, causing a divergence in the estimation. A solution of this problem has been presented in [7] at the cost of introducing an additional parameter c that has to be carefully tuned.

We propose here to use a QR decomposition-based RLS (QR-RLS) algorithm that can address this instability phenomena. Instead of working with the inverse correlation matrix of the input signal, the QR-RLS algorithm performs QR decomposition directly on the correlation matrix of the input signal. Therefore, this algorithm guarantees the property of positive definiteness and is more numerically stable than the standard RLS algorithm.

For use in standard least squares minimization, the QR decomposition of the $l \times n$ matrix $\boldsymbol{A}$ is given by

$$\boldsymbol{Q}\boldsymbol{A} = \begin{pmatrix} \boldsymbol{R} \\ \boldsymbol{0}_{(l-n)\times n} \end{pmatrix}, \tag{44}$$

where $\boldsymbol{Q}$ is a $l \times l$ orthogonal matrix and $\boldsymbol{R}$ is an $n \times n$ upper triangular matrix. Applying the same unitary matrix $\boldsymbol{Q}$ to the data vector $\boldsymbol{b}$

$$\boldsymbol{Q}\boldsymbol{b} = \begin{pmatrix} \boldsymbol{p} \\ \star \end{pmatrix} \tag{45}$$

we obtain the n-dimensional vector $\boldsymbol{p}$ (a $\star$ represents the remaining unused values). The offline estimation (42) is then obtained as

$$\hat{\boldsymbol{\xi}} = \boldsymbol{R}^{-1}\boldsymbol{p}. \tag{46}$$

In the on-line recursive algorithm, QR-RLS updates the matrix $\boldsymbol{R}_k$ each time step k using the relation [28]

$$\widehat{\boldsymbol{Q}}_k \begin{pmatrix} \lambda \boldsymbol{R}_{k-1} \\ \boldsymbol{F}_k \end{pmatrix} = \begin{pmatrix} \boldsymbol{R}_k \\ \boldsymbol{0}_{1\times n} \end{pmatrix}, \tag{47}$$

where $\lambda \in [0, 1]$ is the so-called forgetting factor (tipically, larger than 0.95) used to discount older samples, and thus increasing the estimator adaptability to non-constant parameters. Note that $\widehat{\boldsymbol{Q}}_k$ is a $(n+1)\times(n+1)$ matrix, and its dimension does not increase with new samples. The QR decomposition (47) can be recursively updated using a series of Givens rotations to zero out the non-zero elements on and below the diagonal due to the added row $\boldsymbol{F}_k$. The orthogonal matrix $\widehat{\boldsymbol{Q}}_k$ is used then to update $\boldsymbol{p}_k$ as

$$\widehat{\boldsymbol{Q}}_k \begin{pmatrix} \lambda \boldsymbol{p}_{k-1} \\ \int_0^{t_k} \tau ds \end{pmatrix} = \begin{pmatrix} \boldsymbol{p}_k \\ \star \end{pmatrix}, \tag{48}$$

where an obvious recursive expression can be given also to the integral of the input torque on the left-hand side. Finally, the on-line parameter estimation is

$$\hat{\boldsymbol{\xi}}_k = \boldsymbol{R}_k^{-1} \boldsymbol{p}_k, \tag{49}$$

and the stiffness estimate at time $t = t_k$ is obtained using (43) with the current parameter vector $\hat{\boldsymbol{\alpha}}_k$.

It should be noted that an initialization phase of n samples is needed to set up a complete $\boldsymbol{R}_n$ matrix to be used in the recursive estimation. The QR-RLS algorithm is not only robust with respect to poor excitation, but it is also simple to tune, being the forgetting factor λ the only parameter to be chosen.

4.2 Results with ideal input-output signals

To show the effectiveness of the proposed method, we present simulations on the VSA-II device developed by the University of Pisa [41]. The nonlinear flexibility torque of the two transmissions of the VSA-II is modeled as

$$\tau_{e,i}(\phi_i) = 2k_i\, \beta(\phi_i)\, \frac{\partial \beta(\phi_i)}{\partial \phi_i}, \qquad i = 1, 2, \tag{50}$$

where k_i is the (constant) stiffness of the spring in the i-th transmission, and

$$\beta(\phi_i) = \arcsin\left(C_i \sin\left(\frac{\phi_i}{2}\right)\right) - \frac{\phi_i}{2}, \qquad i = 1, 2, \tag{51}$$

being $C_i > 1$ a geometric parameter of the 4-bar mechanisms, and k_i the stiffness of the internal spring. Due to the antagonistic arrangement, the total flexibility torque acting on the link dynamics is given by the simple sum in eq. (6). For this reason, and with no loss of generality, we will present just the estimation results for a single transmission of this device.

The VSA-II dynamic model is given by eqs. (4–5), and its nominal parameter data were presented in [41]. In particular, the nominal values for the motor parameters were set there to be $B_N = 7.3$ [Kg·m·mm] and $D_{\theta,N} = 1$ [N·mm·s/rad].

FInally, to simulate a non-constant characteristic for the flexible transmission. we have introduced a small time drift to the spring stiffness value k_1,

$$k_1 = k_{1,N} + 0.0005\, t \text{ [N·mm/rad]},$$

where $k_{1,N} = 500$ [N·mm/rad] is the nominal spring stiffness found in [41].

Stiffness estimation methods that need the availability of motor data will use the above nominal data B_N and $D_{\theta,N}$. However, in the actual model used in the simulations we have taken values B_A and $D_{\theta,A}$ for the motor parameters that are slightly off the nominal ones, mimicking the situation of a small (but realistic) error in the off-line identification phase of the motor dynamics. The actual values considered (or, the ground truth in the simulations) were $B_A = 7.5$ [Kg·m·mm] and $D_{\theta,A} = 0.9$ [N·mm·s/rad].

In the first set of simulations, ideal input and output signal have been considered. Thus, we assume that the actual q, θ, and $\dot{\theta}$ are measured and no noise or approximation is introduced on the driving torques τ_i. The two motors apply the sinusoidal torques $\tau_1(t) = 50 \cdot \sin 0.1\pi t$ and $\tau_2(t) = 50 \cdot \sin 2\pi t$ [N·mm], respectively. The simulation runs with a sampling time $T_s = 1$ ms, starting from $q(0) = \theta_1(0) = \theta_2(0) = 0$ [rad] (lower equilibrium configuration), moving under gravity (in the vertical plane) and with the system initially at rest. In the fitting function (37), we used $m = 7$ polynomial terms $f_i(\phi) = \phi^i$. The forgetting factor in the QR-RLS algorithm has been set to $\lambda = 0.98$.

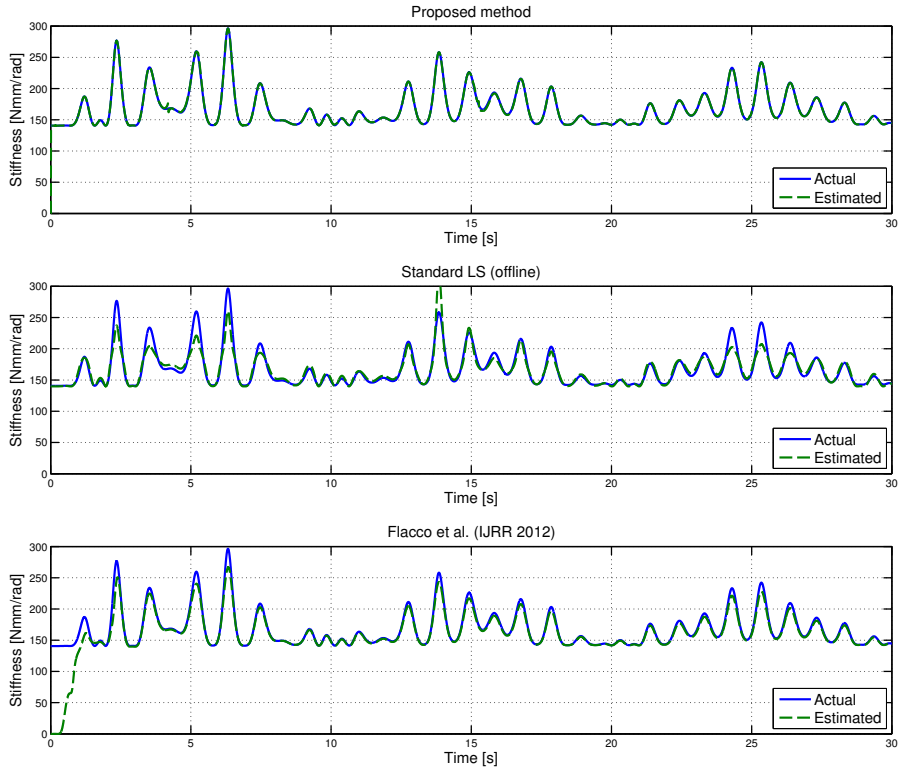

Figure 6: Stiffness estimation for one of the two transmissions of the VSA-II device, using three different methods: Actual stiffness σ (solid, blue) and estimated $\hat{\sigma}$ (dashed, green)

Figure 6 shows the results for the stiffness estimation obtained with the proposed method, compared to a standard off-line Least Squares method and to the residual/RLS-based on-line estimator presented in [9]. It is rather evident that the newly proposed method outperforms the other two. In fact, the standard LS, which considers the whole data set in the estimation of parameters assumed constant, is not able to track the time variation of the transmission flexibility. On the other hand, the method proposed by Flacco et al. [9] works with the assumed nominal motor parameters, and so an imperfect identification of these parameters is reflected in an error on the estimated stiffness. Moreover, the present method returns also estimates of the motor parameters that are very close to the actual ones, namely $\hat{B} = 7.5135$ [Kg·m·mm] and $\hat{D}_\theta = 0.9148$ [N·mm·s/rad].

To quantify the performance of stiffness estimation, we have considered the same two estimation error

indices of Sect. 3, namely the MSE and the (dimensionless) MSREP, both taken over $l_{fin} - l_{in} > 0$ samples:

$$\text{MSE} = \frac{\sum_{k=l_{in}}^{l_{fin}} \left[(\sigma_k - \hat{\sigma}_k)^2 \right]}{l_{fin} - l_{in}}, \qquad \text{MSREP} = \frac{\sum_{k=l_{in}}^{l_{fin}} \left[\left(\frac{\sigma_k - \hat{\sigma}_k}{\sigma_k} \right)^2 \right]}{l_{fin} - l_{in}} \cdot 100. \tag{52}$$

In the evaluation of these two indices, the first $l_{in} = 2000$ samples have been discarded, corresponding to the first 2 s of simulation data, so as to avoid the strong influence of an initial transient phase. The comparative values of the indices are given in Tab. 3.

	Proposed method	Standard LS	Flacco et al. [9]
MSE [N·mm^2/rad^2]	0.58	102.64	31.60
MSREP [%]	0.002	0.224	0.07

Table 3: Performance of stiffness estimation for the VSA-II

4.3 Dealing with signal noises

The presence of noise on input and output signals has to be taken into account in a realistic model of an actuator with flexible transmission (or a VSA). For the torque input τ we can assume a white Gaussian noise with zero mean, while noise on the outputs q and θ will depend on the type of sensor we would like to consider. For instance, white noise was assumed in [29], while the presence of noise due to quantization and discretization of the encoders was considered in [9].

In [9], a Modified Kinematic Kalman Filter (MKKF) was used to filter the encoder quantization noise. The MKKF is a causal filter that outputs a smoothed version of the input signal and a good estimation of its first time derivative, when the SNR is adequate. On the other hand, the stiffness estimator based on operational calculus introduced in [29] and its refined version using modulating functions presented in Sec. 3 result both in a series of non-causal FIR filters on signals that will be feeded in the subsequent RLS algorithm.

After some testing and analysis of these non-causal filtering methods, we realized that their success relies on the validity of two operative conditions:

1. The same non-causal action is applied to all signals used in the RLS algorithm.

2. The characteristics of the flexible transmissions are quasi-constant (namely, can change only very slowly).

The FIR filtering action is applied to a moving window W of data, and the resulting value is assigned as output to the center instant of this window. Thus, when working on-line, the filtered value has a time delay of $T\frac{W}{2}$. Despite this delay, a very effective filtering action is achieved, because of the possibility of considering both previous and successive data. Condition 1 implies that, by having the same time delay for all signals used in the polynomial fitting, the estimate the parameter vector $\boldsymbol{\alpha}$ will inherit the same time delay: namely, at step k we would estimate $\hat{\boldsymbol{\alpha}}_{k-(W/2)}$. From Condition 2 it follows that we can assume $\boldsymbol{\alpha}_k \simeq \hat{\boldsymbol{\alpha}}_{k-(W/2)}$.

With the above in mind, we propose here to introduce two separate filtering actions: a non-causal filter, so as to obtain a robust estimation of the input/output signals to be used in the QR-RLS algorithm; and a causal filter, in order to get a non-delayed smoothed value of ϕ to be used in eq. (43) for the estimation of the current stiffness.

The filtered transmission deformation $\hat{\phi}_k$ can be obtained by two Kinematic Kalman Filters (KKF), one on the motor position θ and one on the link position q. Let x be a generic angular position and $\dot{x}$ the associated angular velocity. In order to estimate $\boldsymbol{\psi}(k) = \boldsymbol{\psi}(t_k) = (x(k)\,\dot{x}(k))^T$ with a KKF, we define

$$\boldsymbol{\psi}(k) = \begin{pmatrix} 1 & T \\ 0 & 1 \end{pmatrix} \boldsymbol{\psi}(k-1) + \boldsymbol{\mu}(k) \tag{53}$$

$$z(k) = \begin{pmatrix} 1 & 0 \end{pmatrix} \boldsymbol{\psi}(k) + \nu(k), \tag{54}$$

where $z(k)$ is the noisy sampled measure (the encoder angle in our case), and $\boldsymbol{\mu}(k)$ and $\nu(k)$ are discrete-time realizations of zero mean Gaussian noises having, respectively, covariance matrix $\boldsymbol{Q}$ and variance R. In the state equation (53), acceleration is not considered and $\boldsymbol{\mu}$ represents also the noise due to this absence. By defining $\boldsymbol{\Gamma} = \begin{pmatrix} T^2/2 & T \end{pmatrix}^T$, the covariance matrix of $\boldsymbol{\mu}$ is $\boldsymbol{Q} = V_a\,\boldsymbol{\Gamma}\boldsymbol{\Gamma}^T$, where V_a is the variance associated to the state. While the variance R of the measures is usually set to a constant value if the noise is Gaussian, in the case of encoder quantization the Modified KKF proposed in [9] should be used instead.

A Savitzky-Golay (SG) non-causal filter [40] is applied to the data needed as inputs to the QR-RLS, namely q, θ, and τ. This digital filter is applied to a window W of measured data and is able to obtain their smoothing, by increasing the signal-to-noise ratio without largely distorting the signal. This is achieved by fitting low-degree polynomials to successive sub-sets of adjacent data points. When the data points are equally spaced, as in our case, an analytical solution to the least squares fitting can be found, in the form of a single set of coefficients that can be applied to all data sub-sets. The filter output provides smoothed estimates of the input signal (and of derivatives of the smoothed signal) at the central point of each data sub-set. The QR-RLS applied on SG filtered data results in a very robust estimation of the parameter vector $\hat{\boldsymbol{\alpha}}_{k-(W/2)}$, despite this comes at the price of a time delay of $T\frac{W}{2}$ seconds.

Assuming that conditions 1) and 2) are satisfied, stiffness estimation is obtained by putting together the two filtered information:

$$\sigma_k \simeq \sum_i^m \hat{\alpha}_{\left(i,k-\frac{W}{2}\right)} g_i(\hat{\phi}_k). \tag{55}$$

4.4 Results with realistic signals

To show the effectiveness of the proposed approach and its robustness with respect to noise, we have compared it with two state-of-the-art stiffness estimators.

The first one is the residual-based stiffness estimator [9]. We have simulated the same VSA-II model under the same operative and design conditions: encoder quantization, white noise on the motor torques, torque input profiles, polynomials used for the fitting, etc. The same causal MKKF used in [9] was applied to estimate $\hat{\phi}$, and a SG filter with a window of 1 second ($W = 1000$ samples at $T_s = 0.001$ s) and a 20-th degree polynomial for estimating the QR-RLS inputs. The forgetting factor was not considered ($\lambda = 1$).

The total stiffness estimated with the present method shows a good quality, see Fig.7. The result is qualitatively similar to the one obtained in [9], while a quantitative comparison can be done by looking at the indices MSE and MSREP as defined in (52). Here, we obtained

$$\text{MSE} = 2.0919\,[\text{N·mm}^2/\text{rad}^2] \quad \text{and} \quad \text{MSREP} = 0.5162\,\%,$$

while in [9] the result was

$$\text{MSE} = 92.2\,[\text{N·mm}^2/\text{rad}^2] \quad \text{and} \quad \text{MSREP} = 0.046\,\%.$$

In addition, the new method provides also a good estimate of the motor parameters: $\hat{B}_1 = 7.2360$ and $\hat{B}_2 = 7.3022$ [Kg·m·mm]; $\hat{D}_{\theta,1} = 0.9731$ and $\hat{D}_{\theta,2} = 0.9980$ [N·mm·s/rad].

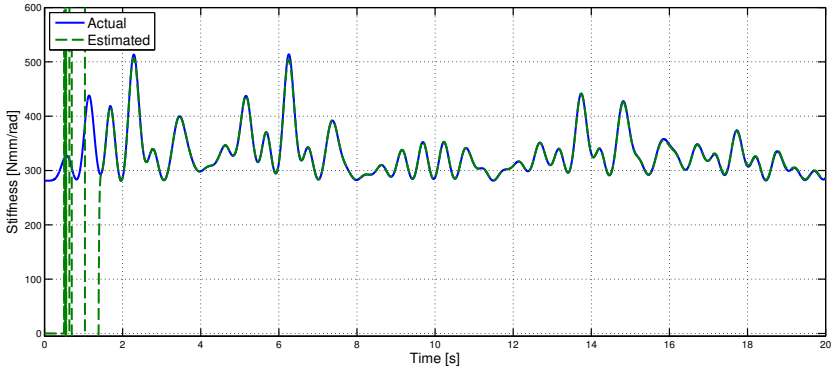

Figure 7: Estimation of the total stiffness of the VSA-II device, when modeled and controlled under the same realistic conditions as in [9]: Actual stiffness σ (solid, blue) and estimated $\hat{\sigma}$ (dashed, green)

The second work taken into account is [29], where an antagonistic VSA with cubic flexibility torques has been considered. Also in this case, we simulated the same model ($B = 10^{-4}$, $D_\theta = 1.27$, etc.), using the same fitting polynomials and torque inputs, and under the same operative conditions (heavy white noise on all signals). We used the KKF to estimate $\hat{\phi}$ with $V_a = 10^{10}$ and $R = 10^4$, and a SG filter with a window of 1 second ($W = 1000$) and a polynomial of the 20-th degree polynomial for estimating the QR-RLS inputs. The forgetting factor was set again to $\lambda = 1$.

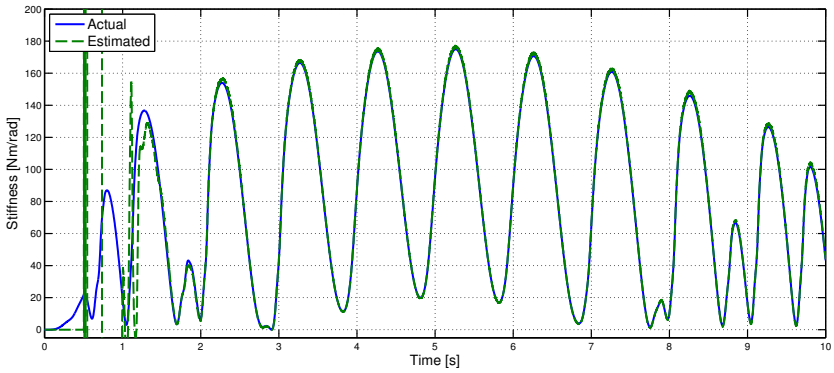

Figure 8: Stiffness estimation for the antagonistic VSA with cubic flexibility torques considered in [29]: Actual stiffness σ (solid, blue) and estimated $\hat{\sigma}$ (dashed, green)

Estimation of the total stiffness is shown in Fig.8. The numerical comparison of the estimation performance indices yields for the present method

$$\text{MSE} = 1.2583\,[\text{N·mm}^2/\text{rad}^2] \quad \text{and} \quad \text{MSREP} = 1.6936\,\%,$$

while in [29] the result was

$$\text{MSE} = 4.2\,[\text{N·mm}^2/\text{rad}^2] \quad \text{and} \quad \text{MSREP} = 0.7\,\%.$$

In the present case, good estimates were found also for the a priori unknown motor parameters: $\hat{B}_1 = 0.0023$, $\hat{B}_2 = 7.1942 \times 10^{-4}$, $\hat{D}_{\theta,1} = 1.2843$, and $\hat{D}_{\theta,2} = 1.2706$.

It is difficult to assess in general the superiority of one method over the other in terms of performance, especially when just looking at a single or few simulations. Nonetheless, we can at least conclude that the present method has the same stiffness estimation quality of state-of-the-art algorithms, while it does not rely on the knowledge of motor parameters (actually, of any physical parameter).

5 Damping estimation

We move next to another issue in the characterization of general Variable Impedance Actuators (VIA), namely estimation of the total damping of the device. Indeed no sensor exists for measuring physical impedance, nor for measuring its specific individual elements: stiffness and damping. As we have seen in the previous Sects. 3 and 4, there is active on-going research focusing on the design and implementation of stiffness estimators for VSA, as a follow-up of the works [7, 9, 12].

On the other hand, Variable Physical Damping Actuation (VPDA) has been lately investigated as a complement to compliant actuators [22]. In these actuators, the transmission damping can be regulated on demand. However, no physical damping estimation algorithms exist at present. Similar to the use of stiffness estimation, an estimation method of the device damping would be certainly useful for feedback control purposes, as well as for diagnostics. We summarize here the method proposed in the submitetd paper [19].

5.1 Estimation of damping in VPDA

We present a damping estimation method that employs a robust RLS algorithm. The method is based only on the measured dissipation torque and on the transmission deformation velocity, which is derived from the measured deformation angle.

Consider a generic damping element embedded in a mechanical system, generating a dissipation torque τ_d which depends in general on its displacement z and velocity $\dot{z}$, and on the control input u to the damping element. The corresponding damping $D > 0$ of this element can be expressed as

$$D(z, \dot{z}, u) = \frac{\partial \tau_d(z, \dot{z}, u)}{\partial \dot{z}}, \tag{56}$$

in which the dissipation torque is assumed to be an odd function with respect to the velocity, i.e.,

$$\tau_d(z, -\dot{z}, u) = -\tau_d(z, \dot{z}, u). \tag{57}$$

We can formulate an estimation problem in which the output signal, namely the (scalar) dissipation torque τ_d, is recursively estimated by a linear adaptive filter with n unknown coefficients $\boldsymbol{w} = (w_1, \ldots, w_n)^T$ and n input signals $\boldsymbol{v} = (v_1, \ldots, v_n)^T$, which can be functions of other system readings. The input-output linear model is then expressed at discrete-time instants $t_i = iT_s$, for $i = 1, 2, \ldots$, by

$$\tau_d(i) = \boldsymbol{v}^T(i)\boldsymbol{w}^* + \xi(i), \tag{58}$$

where $\boldsymbol{w}^*$ is the optimal solution in the mean squares sense and xi is a zero-mean white Gaussian noise sequence with variance σ^2.

The dissipation torque is then approximated by a polynomial function of the damper velocity $\dot{z}$ that satisfies the skew-symmetric condition (57). Therefore, the elements of the input signal vector are expressed by

$$v_j = \dot{z}^{2j-1} \quad \text{for } j = 1, \ldots, n. \tag{59}$$

Similarly to the stiffness estimation case, the damping D can then be obtained from (56) by analytical derivation as

$$D = \left(\frac{\partial \boldsymbol{v}}{\partial \dot{z}}(i)\right)^T \boldsymbol{w} = (\boldsymbol{v}'(i))^T \boldsymbol{w}, \tag{60}$$

where the elements of $\boldsymbol{v}'$ are

$$v'_j = (2j-1)\,\dot{z}^{2j-2} \quad \text{for } j = 1, \ldots, n. \tag{61}$$

Given $m > n$ data points, the relation (58) leads to the over-constrained linear system

$$\boldsymbol{\tau}_d = \mathbf{V}\boldsymbol{w}^* + \boldsymbol{\xi}, \tag{62}$$

where $\boldsymbol{\tau}_d = (\tau_d(1), \ldots, \tau_d(m))^T$, $\boldsymbol{\xi} = (\xi(1), \ldots, \xi(m))^T$ and $\mathbf{V} = (\boldsymbol{v}(1), \ldots, \boldsymbol{v}(m))^T \in \mathbb{R}^{m \times n}$.

RLS algorithm Given an estimate of coefficients $\hat{\boldsymbol{w}}$, the prediction error vector $\boldsymbol{\epsilon} \in \mathbb{R}^m$ is defined by

$$\boldsymbol{\epsilon} = \boldsymbol{\tau}_d - \mathbf{V}\hat{\boldsymbol{w}}. \tag{63}$$

Provided that $\mathbf{V}$ is full column rank, minimization of the cost function (LS problem)

$$J(\hat{\boldsymbol{w}}) = \boldsymbol{\epsilon}^T \boldsymbol{\epsilon}, \tag{64}$$

is provided by the LS estimate

$$\hat{\boldsymbol{w}} = \left(\mathbf{V}^T\mathbf{V}\right)^{-1}\mathbf{V}^T\boldsymbol{\tau}_d. \tag{65}$$

The on-line version of this solution leads to the standard RLS estimation algorithm (see, e.g., [38]), which is reported here for the reader's convenience:

$$\epsilon(i) = \tau_d(i) - \boldsymbol{v}^T(i)\hat{\boldsymbol{w}}(i-1) \tag{66}$$

$$r(i) = \boldsymbol{v}^T(i)\mathbf{P}(i-1)\boldsymbol{v}(i) \tag{67}$$

$$\boldsymbol{k}(i) = \frac{\mathbf{P}(i-1)\boldsymbol{v}(i)}{1+r(i)} \tag{68}$$

$$\hat{\boldsymbol{w}}(i) = \hat{\boldsymbol{w}}(i-1) + \boldsymbol{k}(i)\epsilon(i) \tag{69}$$

$$\mathbf{P}(i) = \Big(\mathbf{I} - \boldsymbol{k}(i)\boldsymbol{v}^T(i)\Big)\mathbf{P}(i-1). \tag{70}$$

where r is the modified Kalman residual covariance, $\boldsymbol{k} \in \mathbb{R}^n$ is the modified Kalman gain vector, and $\mathbf{P} \in \mathbb{R}^{m\times m}$ denotes the covariance matrix of the prediction error.

In the stiffness estimation method presented in [9], some instability problems due to the lack of persistent excitation of the standard RLS algorithm were attenuated by using a modification introduced in [3]. In a similar way, equations (69) and (70) can be replaced by

$$\hat{\boldsymbol{w}}(i) = \hat{\boldsymbol{w}}(i-1) + \alpha(i)\boldsymbol{k}(i)\epsilon(i) \tag{71}$$

and

$$\mathbf{P}(i) = \left(\mathbf{I} - \alpha(i)\boldsymbol{k}(i)\boldsymbol{v}^T(i)\right)\mathbf{P}(i-1). \tag{72}$$

where $\alpha(i)$ is a stability factor which is simply selected as in [9],

$$\alpha(i) = c\,\frac{1+r(i)}{1+c\,r(i)}, \tag{73}$$

where $c > 0$ is the stabilizing factor.

Damping estimation algorithm The final algorithm for estimating damping in VPDA is obtained by a suitable modification of the RLS method to account for time-varying conditions.

It is well-known that an exponential forgetting factor can be incorporated as a weighting term in the RLS algorithm, so as to attain faster convergence for time-varying systems, discounting older signals and relying more on recent ones [17]. One way to Include a forgetting factor, is to modify the cost function (64) as

$$J(\hat{\boldsymbol{w}}) = \boldsymbol{\epsilon}^T\mathbf{R}^{-1}\boldsymbol{\epsilon}, \tag{74}$$

where $\mathbf{R} = \text{diag}\{\lambda^{m-1}, ..., \lambda^0\}$ and $\lambda \in (0, 1]$ is the forgetting factor [27].

A further method for enhancing the tracking performance of the RLS algorithm is by using a directional forgetting scheme, in which past data are forgotten solely in those directions of the parameter space from where new information comes [18]. The exponential and directional forgetting RLS algorithm, modified by Bittanti [3] with the goal of achieving a better estimation performance for time-varying parameters, can be described by incorporating a correction factor $\delta \in [0, 0.01]$ in the update of the covariance matrix as

$$\mathbf{P}(i) = \left(\mathbf{I} - \frac{\mathbf{P}(i-1)\boldsymbol{v}(i)\boldsymbol{v}^T(i)}{\beta^{-1}(i) + r(i)}\right)\mathbf{P}(i-1) + \delta\mathbf{I}, \tag{75}$$

where $\beta(i)$ is an auxiliary variable defined as

$$\beta(i) = \begin{cases} \lambda(i) - \dfrac{1-\lambda(i)}{r(i)}, & \text{if } r(i) > 0, \\ 1, & \text{if } r(i) = 0. \end{cases} \tag{76}$$

When $\lambda = 1$, no forgetting effect is applied giving up a more prompt estimation response to time-varying parameters. On the other hand, any decrease of this factor enhances the contribution of latest data on the estimation process (which is good) but also the sensitivity to noise (which is bad) [4]. To cope with this situation, one needs to resort to a variable forgetting factor through monitoring prediction error: when the prediction error grows rapidly, the forgetting factor is progressively decreased down to a minimum value λ_{min}; when the prediction error is small, it is increased up to its maximum value, $\lambda = 1$. Thus, a variable forgetting factor scheme can be expressed as [45]

$$\lambda(i) = \lambda_{min} + (1 - \lambda_{min})\, 2^{L(i)}, \tag{77}$$

with

$$L(i) = -\textit{round}\left(\frac{\rho\epsilon^2(i)}{\eta(i)}\right). \tag{78}$$

where ρ is a design parameter, the function *round*$(.)$ rounds its argument to the nearest integer, and $\eta(i)$ is the energy of an a priori estimation error defined for moderating the sensitivity of the forgetting factor to the dynamic range of the error. The latter is updated as

$$\eta(i) = \lambda_c\eta(i-1) + \epsilon^2(i), \tag{79}$$

being λ_c another constant forgetting factor.

The proposed algorithm is based on the use of a variable weighting factor (77)–(79) in the exponential and directional forgetting RLS algorithm defined by (66)–(69) and (75)–(76). The complete method is summarized in Algorithm 1.

5.2 Experimental results

Experiments were carried out to test the damping estimation algorithm on a VPDA device, the CompAct actuator developed at IIT, see [21]. Excitation of the system is performed through manual motion of the link, while the motor is controlled to maintain a fixed position. To achieve a desired viscous damping D_d in this mechanical system, the normal force applied to the friction plates is modulated so as to emulate a viscous damping behaviour. For ease of implementation, a value $n = 2$ was used in the approximation (59), resulting in a linear-cubic polynomial.

Algorithm 1 Damping estimation algorithm

Parameters: $\lambda_c, \lambda_{min}, \rho, \delta$ and n

Initialization: $\eta(0), \mathbf{P}(0), \boldsymbol{w}(0)$ and $i = 0$

while "systems is running" **do**

$i = i + 1$

input $\tau_d(i), \dot{z}$

$\boldsymbol{v}(i) = (\dot{z}, \ldots, \dot{z}^{2n-1})^T$

$\epsilon(i) = \tau_d(i) - \boldsymbol{v}^T(i)\hat{\boldsymbol{w}}(i-1)$

$\eta(i) = \lambda_c \eta(i-1) + \epsilon^2(i)$

$L(i) = -\mathit{round}(\rho \epsilon^2(i)/\eta(i))$

$\lambda(i) = \lambda_{min} + (1 - \lambda_{min}) \cdot 2^{L(i)}$

$r(i) = \boldsymbol{v}^T(i)\mathbf{P}(i-1)\boldsymbol{v}(i)$

if $r(i) > 0$ **then**

$$\beta(i) = \lambda(i) - \frac{1 - \lambda(i)}{r(i)}$$

else

$\beta(i) = 1$

end if

$$\boldsymbol{k}(i) = \frac{\mathbf{P}(i-1)\boldsymbol{v}(i)}{1 + r(i)}$$

$\hat{\boldsymbol{w}}(i) = \hat{\boldsymbol{w}}(i-1) + \boldsymbol{k}(i)\epsilon(i)$

$\hat{\tau}_d(i) = \boldsymbol{v}^T(i)\hat{\boldsymbol{w}}(i)$

$\boldsymbol{v}'(i) = \left(1, \ldots, (2n-1)\dot{z}^{2n-2}\right)^T$

$\hat{D}(i) = \boldsymbol{v}'^T(i)\hat{\boldsymbol{w}}(i)$

$$\mathbf{P}(i) = \left(\mathbf{I} - \frac{\mathbf{P}(i-1)\boldsymbol{v}(i)\boldsymbol{v}^T(i)}{\beta^{-1}(i) + r(i)}\right)\mathbf{P}(i-1) + \delta\mathbf{I}$$

output $\hat{\tau}_d(i), \hat{D}(i)$

end while

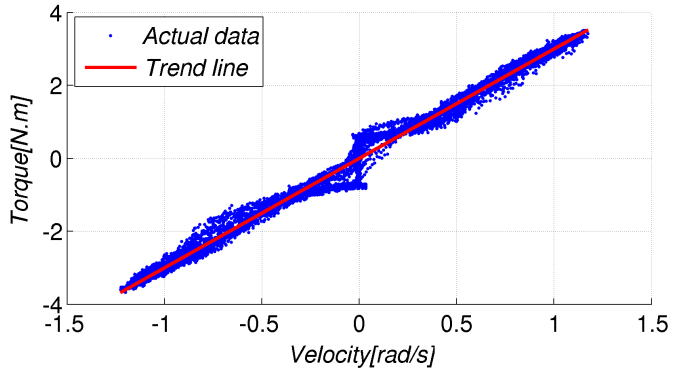

Figure 9: Variation in dissipation torque vs. relative velocity of friction plates

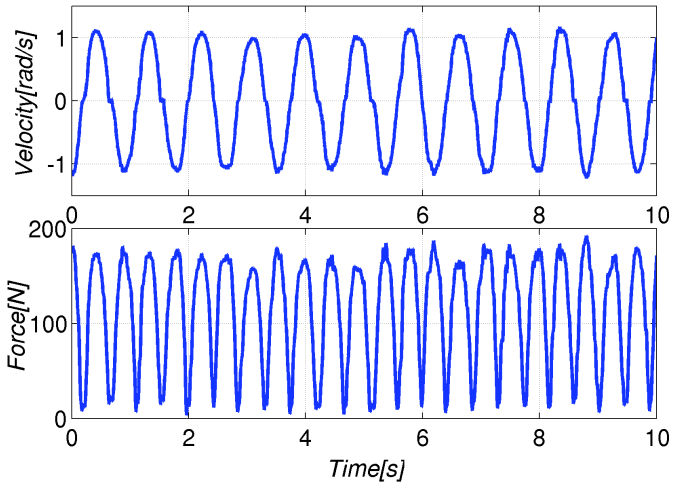

Figure 10: Time evolution of the clutch normal force and of the relative velocity of clutch plates

Constant damping The first experiment consists in estimating a desired constant viscous damping behaviour, as specified by $D_d = 3$ [Nm s/rad]. Figure 9 shows the variation in dissipation torque versus the change in relative velocity of the friction plates. Since a constant damping was regulated, based on (56) the slope of the trend-line of this graph provides a value $D = 3.02$ Nms/rad with Normalized Root Mean Squared Error (NRMSE) of 2.74%, representing a suitable approximation of the real damping in the system.

The estimation of the constant damping using the proposed approach provided a NRMSE of 2.89%, which is quite close to the previous value. The time evolution of the friction force applied by the clutch plates and the relative velocity of the plates are shown in Fig. 10. The behaviour of the estimated torque in comparison to the measured one is reported in Fig. 11, together with the normalized error between the two. The normalized error is below 1%, showing the good accuracy of the estimation.

Figure 12 represents the evolution in time of the coefficients w_1 (weighting the linear velocity term) and w_2 (weighting the cubic velocity term) of the approximating polynomial, the desired constant damping, the (slightly oscillatory) estimated one, and the percentage error between the two. The last plot shows that this error reaches a maximum of about 5%, being mostly due to unmodelled friction around the zero-velocity area (the effect of stiction on the dissipation torque around the origin can also be observed in Fig. 9).

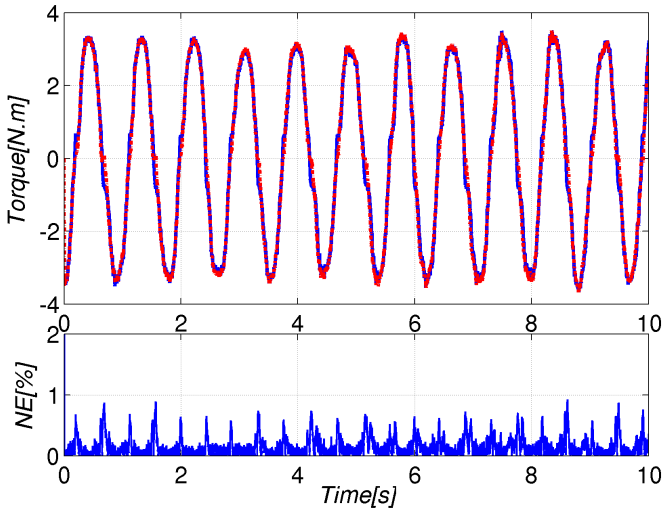

Figure 11: Time evolution of measured (solid, blue) and estimated (dashed, red) dissipation torque [top], and the normalized error between the two [bottom]

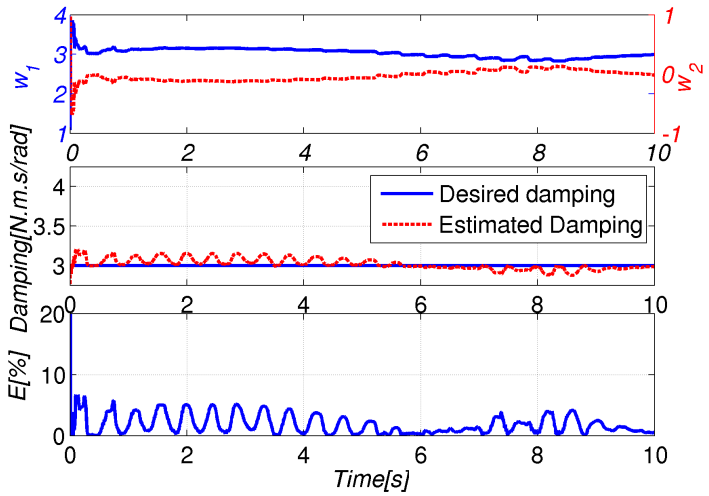

Figure 12: Time evolution of the two coefficients w_1 (blue) and w_2 (red) in the polynomial approximation [top], constant desired (blue) and estimated (red) damping [center], and the error between the two [bottom]

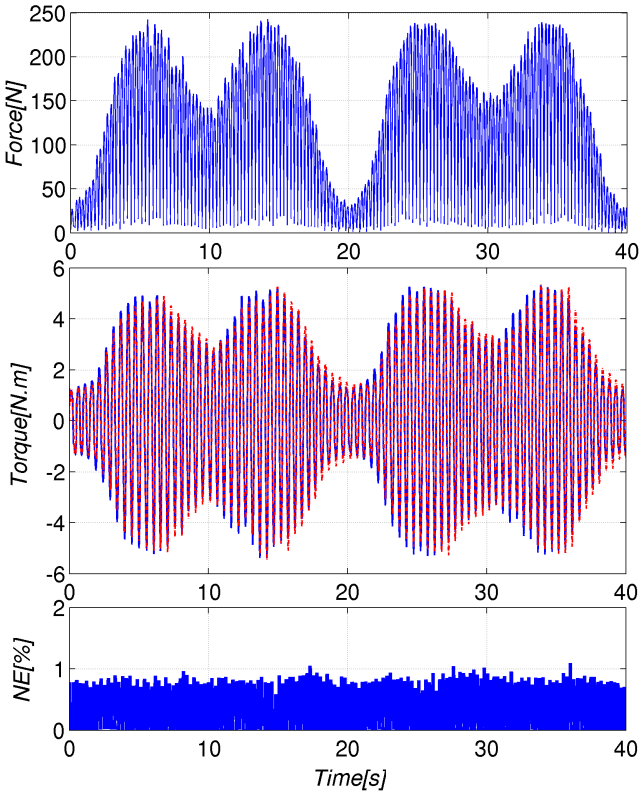

Figure 13: Time evolution of the clutch normal force [top], measured (blue, solid) and estimated (red, dashed) dissipation torques [center] and the normalized error between the two [bottom]

Time-varying damping In this second experiment, the normal force applied on the friction plates is modulated so as to produce a desired time-varying damping, as specified by by

$$D_d(t) = 1 + 1.4\sin^2(0.05\pi\, t) + 1.7\sin^2(0.1\pi\, t). \tag{80}$$

The results obtained using the damping estimation algorithm provide in this case a value NRMSE of 3.17%. Figure 13 shows the force applied to friction plates, the measured and estimated torque, in addition to the corresponding normalized error between measured and estimated torques. The error in this experiment is also below 1% validating the accuracy of estimation when compared to the actual value.

Figure 14 collects the time evolutions of all the relevant quantities. It can be seen that error between reference and estimated values varies from less than 10% in the domain of high damping to about 30% for damping of lower magnitudes. This is comparable with the accuracy of the identified friction model in response to low and high forces.

6 Stabilizing cyclic motions in VSA systems

Intrinsic elasticities in biological and robotic multi-body systems enable the execution of highly dynamic and complex motions, such as hitting and throwing, or walking and running. The compliant actuator behavior improves the mechanism robustness during rigid contacts with the environment and increases performance and energy efficiency. However, the generation of effective and efficient motions is not trivial.

In this section, we aim at robustly controlling periodic motions for robotic systems with Variable Stiffness Actuation (VSA) [46, 1, 11]. The idea is to exploit the natural dynamics of these systems and to control them so

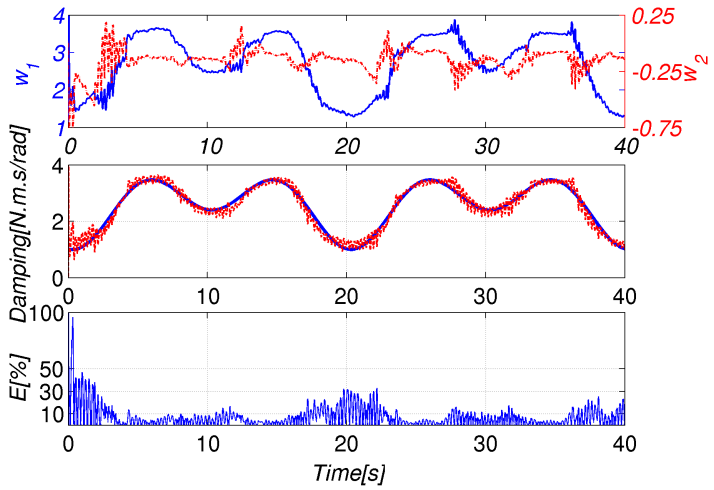

Figure 14: Time evolution of the two coefficients w_1 (blue, solid) and w_2 (red, dashed) in the polynomial approximation [top], reference (blue, solid) and estimated (red, dashed) damping [center], and the error between the two [bottom]

that they are able to robustly handle external disturbances (such as robot-ground contacts) in a similar way as their biological archetype. The underlying assumption is that these systems feature intrinsically some internal nonlinear oscillation modes, which correspond to the mentioned dynamic motion patterns. The goal is to find appropriate control strategies, that first enables to identify and then will excite one of these oscillation modes. To this end, we propose two different control approaches.

The first approach, detailed in Sect. 6.1), achieves a desired dynamical behavior by means of a control law and then decouples the closed-loop dynamics in terms of modal coordinates, constraining the motion of the robot to some invariant manifold of its state space. Using these dynamic constraints, we will be able to stabilize limit cycles along one of the resulting oscillation modes, which is as close as possible to the natural dynamics of the plant.

The second approach, presented in Sect. 6.2), extends the single-input single-output controller introduced in [25] to the multi-input multi-output case. This is achieved by an adaptive part which converges to a coordinate transformation of the dominant oscillation mode of the robotic plant. The coordinate transformation is then used to modally distribute the energy input over the joints, thereby increasing effectiveness in the excitation of limit cycles.

6.1 Modal decoupling and limit cycle control

The concept of modal decoupling is best introduced by considering first the dynamics of a rigid robot manipulator, i.e.,

$$\boldsymbol{M}(\boldsymbol{q})\ddot{\boldsymbol{q}} + \boldsymbol{C}(\boldsymbol{q},\dot{\boldsymbol{q}})\dot{\boldsymbol{q}} + \boldsymbol{g}(\boldsymbol{q}) = \boldsymbol{\tau}. \tag{81}$$

As a matter of fact, this model mimics closely the link dynamics (9) of a multi-dof VSA-driven robot. The only apparent difference is in the right-hand side, where the flexibility torques $\boldsymbol{\tau}_e$ of the VSA case are replaced here by the commanded motor torques $\boldsymbol{\tau}$ of the rigid case.

Starting then with the robot dynamics (81), assume that the following PD control law with additional terms to compensate for Coriolis/centrifugal and gravity effects is applied

$$\boldsymbol{\tau} = \boldsymbol{u}_q + \boldsymbol{C}(\boldsymbol{q},\dot{\boldsymbol{q}})\dot{\boldsymbol{q}} + \boldsymbol{g}(\boldsymbol{q}) + \boldsymbol{M}(\boldsymbol{q})\ddot{\boldsymbol{q}}_d - \boldsymbol{D}_d(\boldsymbol{q})\dot{\tilde{\boldsymbol{q}}} - \boldsymbol{K}_d(\boldsymbol{q})\tilde{\boldsymbol{q}}, \tag{82}$$

where $\tilde{\boldsymbol{q}} = \boldsymbol{q} - \boldsymbol{q}_d$ is the tracking error with respect to a desired trajectory $\boldsymbol{q}_d(t)$, $\boldsymbol{D}_d(\boldsymbol{q})$ and $\boldsymbol{K}_d(\boldsymbol{q})$ are symmetric, positive definite (and possibly diagonal) damping and stiffness matrices, and we have introduced an auxiliary control input $\boldsymbol{u}_q$ for later use. Note that the impedance controller (82), when $\boldsymbol{u}_q = \boldsymbol{0}$, is able to asymptotically track any desired smooth trajectory $\boldsymbol{q}_d(t)$. Substituting eq. (82) in (81), leads to the closed-loop error dynamics

$$\boldsymbol{M}(\boldsymbol{q})\ddot{\tilde{\boldsymbol{q}}} + \boldsymbol{D}_d(\boldsymbol{q})\dot{\tilde{\boldsymbol{q}}} + \boldsymbol{K}_d(\boldsymbol{q})\tilde{\boldsymbol{q}} = \boldsymbol{u}_q, \tag{83}$$

To derive the decoupling coordinate transformation for system (83), we invoke a result on the generalized eigenvalue problem known from matrix algebra, see [15] and [35].

Lemma 1 *Given a symmetric and positive definite matrix $\boldsymbol{A} \in \mathbb{R}^{n\times n}$ and a symmetric matrix $\boldsymbol{B} \in \mathbb{R}^{n\times n}$, there exist a non-singular matrix $\boldsymbol{W} \in \mathbb{R}^{n\times n}$ and a diagonal matrix $\boldsymbol{B}_W \in \mathbb{R}^{n\times n}$ such that $\boldsymbol{W}^{-T}\boldsymbol{W}^{-1} = \boldsymbol{A}$ and $\boldsymbol{W}^{-T}\boldsymbol{B}_W\boldsymbol{W}^{-1} = \boldsymbol{B}$.*

If we now apply Lemma 1 to $\boldsymbol{A} \triangleq \boldsymbol{M}(\boldsymbol{q})$ and $\boldsymbol{B} \triangleq \boldsymbol{K}_d(\boldsymbol{q})$, we obtain the transformation

$$\boldsymbol{z} = \boldsymbol{W}^{-1}(\boldsymbol{q})\,\tilde{\boldsymbol{q}} \tag{84}$$

which maps the joint error coordinates $\tilde{\boldsymbol{q}}$ to the desired modal coordinates $\boldsymbol{z}$. In order to rewrite system (83) in modal coordinates, we use the inverse of (84) namely

$$\tilde{\boldsymbol{q}} = \boldsymbol{W}(\boldsymbol{q})\boldsymbol{z}. \tag{85}$$

Based on Lemma 1, the desired damping matrix should be designed in modal coordinates, namely as

$$\boldsymbol{D}_d(\boldsymbol{q}) = \boldsymbol{W}^{-T}(\boldsymbol{q})\left(2\,\mathrm{diag}\left\{\xi_i\sqrt{\lambda_i(\boldsymbol{q})}\right\}\right)\boldsymbol{W}^{-1}(\boldsymbol{q}) \tag{86}$$

Here, $\xi_i \geq 0$ are constant, normalized modal damping coefficients, for $i = 1, \ldots, n$.

Substituting (85) in eq. (83), we obtain the modal dynamics

$$\ddot{\boldsymbol{z}} + 2\,\mathrm{diag}\left\{\xi_i\sqrt{\lambda_i(\boldsymbol{q})}\right\}\dot{\boldsymbol{z}} + \mathrm{diag}\left\{\lambda_i(\boldsymbol{q})\right\}\boldsymbol{z} = \boldsymbol{W}^T(\boldsymbol{q})\left(\boldsymbol{u}_q - \boldsymbol{\gamma}\right) \tag{87}$$

being

$$\boldsymbol{I} = \boldsymbol{W}^T(\boldsymbol{q})\,\boldsymbol{M}(\boldsymbol{q})\,\boldsymbol{W}(\boldsymbol{q}) \tag{88}$$

$$\mathrm{diag}\left\{\lambda_i(\boldsymbol{q})\right\} = \boldsymbol{W}^T(\boldsymbol{q})\,\boldsymbol{K}_d(\boldsymbol{q})\,\boldsymbol{W}(\boldsymbol{q}) \tag{89}$$

$$\boldsymbol{\gamma} = \left(\boldsymbol{M}(\boldsymbol{q})\ddot{\boldsymbol{W}}(\boldsymbol{q}) + \boldsymbol{D}_d(\boldsymbol{q})\dot{\boldsymbol{W}}(\boldsymbol{q})\right)\boldsymbol{z} + 2\boldsymbol{M}(\boldsymbol{q})\dot{\boldsymbol{W}}(\boldsymbol{q})\dot{\boldsymbol{z}}. \tag{90}$$

Using in (87) the control law

$$\boldsymbol{u}_q = \boldsymbol{W}^{-T}(\boldsymbol{q})\,\boldsymbol{u}_z + \boldsymbol{\gamma}, \tag{91}$$

being $\boldsymbol{u}_z$ the new control input, we obtain n subsystems in terms of the modal coordinates $\boldsymbol{z}$:

$$\ddot{\boldsymbol{z}} + 2\,\mathrm{diag}\left\{\xi_i\sqrt{\lambda_i(\boldsymbol{q})}\right\}\dot{\boldsymbol{z}} + \mathrm{diag}\left\{\lambda_i(\boldsymbol{q})\right\}\boldsymbol{z} = \boldsymbol{u}_z. \tag{92}$$

To prove stability of the homogeneous closed-loop dynamics (92), we consider a positive definite Lyapunov function candidate V_i for each decoupled subsystem, and deduce stability if each time derivative $\dot{V}_i$ is negative

definite, i.e., $V_i > 0, \forall i \Rightarrow V = \sum_i V_i > 0$, and $\dot{V}_i < 0, \forall i \Rightarrow \dot{V} = \sum_i \dot{V}_i < 0$, $\forall (\boldsymbol{z}^T \, \dot{\boldsymbol{z}}^T)^T \neq \mathbf{0})$. Thus, consider the i-th decoupled subsystem

$$\ddot{z}_i + 2\,\xi_i \sqrt{\lambda_i(\boldsymbol{q})}\dot{z}_i + \lambda_i(\boldsymbol{q}) z_i = 0. \tag{93}$$

With the state vector $\boldsymbol{x}_i = (z_i \;\; \dot{z}_i)^T$, a positive definite Lyapunov function candidate is given by

$$V_i(\boldsymbol{x}_i) = \frac{1}{2}\, \boldsymbol{x}_i^T \begin{pmatrix} c_2 & c_1/2 \\ c_1/2 & 1 \end{pmatrix} \boldsymbol{x}_i, \tag{94}$$

where c_1, c_2 are positive constants and $c_2 > c_1^2/4$. The derivative of the Lyapunov function

$$\dot{V}_i(\boldsymbol{x}_i, \boldsymbol{q}) = -\frac{1}{2}\, \boldsymbol{x}_i^T \boldsymbol{H}_i(\lambda_i(\boldsymbol{q}))\boldsymbol{x}_i, \tag{95}$$

will be negative definite, provided that the matrix

$$\boldsymbol{H}_i(\lambda_i(\boldsymbol{q})) = \begin{pmatrix} c_1\lambda_i(\boldsymbol{q}) & \lambda_i(\boldsymbol{q}) + c_1\xi_i\sqrt{\lambda_i(\boldsymbol{q})} - c_2 \\ \text{symm} & 4\xi_i\sqrt{\lambda_i(\boldsymbol{q})} - c_1 \end{pmatrix} \tag{96}$$

is positive definite. We can conclude that the equilibrium point $\boldsymbol{x}_i = \mathbf{0}$ of (93) is asymptotically stable, if the leading principal minors of $\boldsymbol{H}_i(\lambda_i(\boldsymbol{q}))$ are strictly positive (as functions of $\boldsymbol{q}$, $\forall \boldsymbol{q} \in \mathbb{R}^n$), i.e.,

$$c_1\lambda_i(\boldsymbol{q}) > 0, \tag{97}$$

$$\det\left(\boldsymbol{H}_i(\lambda_i(\boldsymbol{q}))\right) > 0. \tag{98}$$

The proof of the existence of suitable constants c_1, c_2, and a comprehensive analysis of the corresponding stability region are provided in [23].

In the following, we show how to produce an asymptotically stable limit cycle for the generic k-th decoupled system in (92). Setting $\xi_k = 0$ and dividing by $\lambda_k(t) > 0$ (positivity holds $\forall t$), the system becomes

$$\frac{1}{\lambda_k(t)}\, \ddot{z}_k + z_k = \frac{1}{\lambda_k(t)}\, u_{z_k}, \tag{99}$$

with state $(z_k \;\; \dot{z}_k)^T \in \mathbb{R}^2$. Similarly to what was done in [10], consider the scalar function

$$H\left(t, z_k, \dot{z}_k\right) = \frac{1}{2\lambda_k(t)}\, \dot{z}_k^2 + \frac{1}{2}\, z_k^2 \geq 0, \tag{100}$$

with time derivative along the trajectories of (99)

$$\dot{H}\left(t, z_k, \dot{z}_k\right) = \frac{1}{\lambda_k(t)}\, u_{z_k}\dot{z}_k - \frac{\dot{\lambda}_k(t)}{2\lambda_k(t)^2}\, \dot{z}_k^2. \tag{101}$$

Choose the input as

$$u_{z_k} = \lambda_k(t)\left(-k_V \tilde{H}\left(t, z_k, \dot{z}_k\right) \dot{z}_k + \frac{\dot{\lambda}_k(t)}{2\lambda_k(t)^2}\, \dot{z}_k^2\right), \tag{102}$$

where $k_V > 0$, $\tilde{H}\left(t, z_k, \dot{z}_k\right) = H\left(t, z_k, \dot{z}_k\right) - H_d$ and $H_d > 0$, such that the derivative of $H\left(t, z_k, \dot{z}_k\right)$ results in

$$\dot{H}\left(t, z_k, \dot{z}_k\right) = -k_V \tilde{H}\left(t, z_k, \dot{z}_k\right) \dot{z}_k^2. \tag{103}$$

The system (99), unlike the one considered in [10], is non-autonomous and so we cannot apply directly La Salle's theorem. Nevertheless, with a similar argument, we can prove that it has an asymptotically stable limit cycle $\Omega = \{z_k, \dot{z}_k \mid H\left(t, z_k, \dot{z}_k\right) = H_d\}$. It remains to show stability and attractiveness of this limit cycle.

Uniform stability Choosing as Lyapunov function the continuously differentiable function

$$V\left(t, z_k, \dot{z}_k\right) = \frac{1}{2}\tilde{H}\left(t, z_k, \dot{z}_k\right)^2, \tag{104}$$

with

- $V\left(t, \Omega\right) = 0$
- $S_1\left(z_k, \dot{z}_k\right) \leq V\left(t, z_k, \dot{z}_k\right) \leq S_2\left(z_k, \dot{z}_k\right)$
- $\dot{V}\left(t, z_k, \dot{z}_k\right) = -k_V \tilde{H}\left(t, z_k, \dot{z}_k\right)^2 \dot{z_k}^2 \leq 0$

$\forall t \geq 0$ and $\forall\left(z_k, \dot{z}_k\right) \in \mathbb{R}^2$, and where

$$S_1\left(z_k, \dot{z}_k\right) = \frac{1}{2}\left(\frac{1}{2\lambda_{k,\text{max}}}\dot{z}_k^2 + \frac{1}{2}z_k^2 - H_d\right)^2$$

$$S_2\left(z_k, \dot{z}_k\right) = \frac{1}{2}\left(\frac{1}{2\lambda_{k,\text{min}}}\dot{z}_k^2 + \frac{1}{2}z_k^2 - H_d\right)^2$$

are positive definite functions on $\mathbb{R}^2$, we can conclude that Ω is uniformly stable.

Attractiveness Attractiveness is proven using Barbalat's lemma (see, e.g., [43]). We have already shown that $V\left(t, z_k, \dot{z}_k\right)$ is bounded from below and that $\dot{V}\left(t, z_k, \dot{z}_k\right)$ is negative semidefinite. In order to apply Barbalat's lemma, it remains only to show that $\ddot{V}\left(t, z_k, \dot{z}_k\right)$ is bounded. This follows from

$$\ddot{V}\left(t, z_k, \dot{z}_k\right) = -2k_V \tilde{H}\left(t, z_k, \dot{z}_k\right)^2\left(k_V \dot{z}_k + \dot{z}_k \ddot{z}_k\right),$$

which is bounded since (99) is stable. So, we conclude that $\lim_{t\to\infty} \dot{V}\left(t, z_k, \dot{z}_k\right) = 0$. Let $B_\epsilon\left(\Omega\right)$ be a neighbourhood of Ω, such that $\left(z_k = 0, \dot{z}_k = 0\right) \notin B_\epsilon\left(\Omega\right)$. Since Ω is stable, we can choose the initial condition such that the solution remains always in $B_\epsilon\left(\Omega\right)$. Moreover, we have shown that either $\dot{z}_k \to 0$ or $H\left(t, z_k, \dot{z}_k\right) \to H_d$ as $t \to \infty$, but since the system cannot converge to $\left(z_k \neq 0, \dot{z}_k = 0\right)$ and $\left(z_k = 0, \dot{z}_k = 0\right) \notin B_\epsilon\left(\Omega\right)$ then we conclude that the solution can only converge to $\Omega = \left\{z_k, \dot{z}_k \mid H\left(t, z_k, \dot{z}_k\right) = H_d\right\}$.

The last step of our application is the extension to the case of VSA-driven multi-dof robots, as modeled by eqs. (9–11). We will do so by deriving a controller that is able to track any desired flexibility torque $\boldsymbol{\tau}_{e,d}$, using the basic concept of decoupling the flexible joint torque dynamics from the dynamics of the joint position. The approach was proposed in [34] for the case of robots with constant joint stiffness, but allows a rather straightforward extension to the VSA case.

Consider the inversion of the flexibility torque function $\boldsymbol{\psi}$ in (11)

$$\boldsymbol{\theta} - \boldsymbol{q} = \boldsymbol{\psi}^{-1}(\boldsymbol{\tau}_e).$$

Rearranging and differentiating twice w.r.t. time yields

$$\dot{\boldsymbol{\theta}} = \dot{\boldsymbol{q}} + \frac{\partial \boldsymbol{\psi}^{-1}(\boldsymbol{\tau}_e)}{\partial \boldsymbol{\tau}_e}\dot{\boldsymbol{\tau}}_e, \qquad \ddot{\boldsymbol{\theta}} = \ddot{\boldsymbol{q}} + \frac{\partial \boldsymbol{\psi}^{-1}(\boldsymbol{\tau}_e)}{\partial \boldsymbol{\tau}_e}\ddot{\boldsymbol{\tau}}_e + \frac{d}{dt}\left(\frac{\partial \boldsymbol{\psi}^{-1}(\boldsymbol{\tau}_e)}{\partial \boldsymbol{\tau}_e}\right)\dot{\boldsymbol{\tau}}_e. \tag{105}$$

Substituting the acceleration $\ddot{\boldsymbol{\theta}}$ in the motor equation (10) leads to

$$\boldsymbol{B}\left(\frac{\partial \boldsymbol{\psi}^{-1}(\boldsymbol{\tau}_e)}{\partial \boldsymbol{\tau}_e}\ddot{\boldsymbol{\tau}}_e + \frac{d}{dt}\left(\frac{\partial \boldsymbol{\psi}^{-1}(\boldsymbol{\tau}_e)}{\partial \boldsymbol{\tau}_e}\right)\dot{\boldsymbol{\tau}}_e\right) + \boldsymbol{\tau}_e = \boldsymbol{\tau} - \boldsymbol{B}\ddot{\boldsymbol{q}}. \tag{106}$$

If a desired flexibility torque profile $\boldsymbol{\tau}_{e,d}(t)$ has to be tracked at the joints, then the control input $\boldsymbol{\tau} \in \mathbb{R}^m$ will be chosen as

$$\boldsymbol{\tau} = \boldsymbol{\tau}_{e,d} + \boldsymbol{B}\ddot{\boldsymbol{q}} + \boldsymbol{B}\,\frac{d}{dt}\left(\frac{\partial \boldsymbol{\psi}^{-1}(\boldsymbol{\tau}_e)}{\partial \boldsymbol{\tau}_e}\right)\dot{\boldsymbol{\tau}}_e + \boldsymbol{B}\,\frac{\partial \boldsymbol{\psi}^{-1}(\boldsymbol{\tau}_e)}{\partial \boldsymbol{\tau}_e}\left(\ddot{\boldsymbol{\tau}}_{e,d} + \boldsymbol{D}_\tau \dot{\boldsymbol{e}}_\tau + \boldsymbol{K}_\tau \boldsymbol{e}_\tau\right), \tag{107}$$

where $\boldsymbol{e}_\tau = \boldsymbol{\tau}_{e,d} - \boldsymbol{\tau}_e$ is the control error and $\boldsymbol{K}_\tau$, $\boldsymbol{D}_\tau$ are symmetric and positive definite gain matrices. Note that the link acceleration$\ddot{\boldsymbol{q}}$ required in (107) can be obtained from (9), since the flexiblity torques $\boldsymbol{\tau}_e$ can be measured by a joint torque sensor. The control error dynamics becomes

$$\ddot{\boldsymbol{e}}_\tau + \boldsymbol{D}_\tau \dot{\boldsymbol{e}}_\tau + \left(\boldsymbol{K}_\tau + \left(\frac{\partial \boldsymbol{\psi}^{-1}(\boldsymbol{\tau}_e)}{\partial \boldsymbol{\tau}_e}\right)^{-1}\boldsymbol{B}^{-1}\right)\boldsymbol{e}_\tau = \boldsymbol{0}, \tag{108}$$

showing that asymptotical stability of $\boldsymbol{e}_\tau$ can be achieved by proper tuning of the control gains.

As a result, the modal limit cycle dynamics can be implemented for the VSA system (10)–(11) by simply plugging as $\boldsymbol{\tau}_{e,d}$ in (107) the right hand-side of eq. (82), in which (91) and (102) are also used.

6.2 Modal adaptive bang-bang control

Our goal here is to control periodic motions of the link position coordinates $\boldsymbol{q} \in \mathbb{R}^n$ in a VIA-driven robot using the bang-bang control introduced in [25]. Since that controller accounts only for scalar quantities, we seek a transformation such that the motion $\boldsymbol{q}(t)$ can be represented by a single coordinate, for instance, $y_1(t)$. The basic idea can be explained in the context of differential geometry (see also the sketch in Fig. 15(a)).

Consider the time series of joint positions $\boldsymbol{q}(t)$ representing the motion of the multi-joint robot, where $\boldsymbol{q} \in Q \subset \mathbb{R}^n$ are coordinates of a manifold Q. Assume that we can represent the trajectory $\boldsymbol{q}(t)$ on a lower dimensional manifold Y, with coordinates $\boldsymbol{y} \in Y \subset \mathbb{R}^p$, with $p \leq n$ (in particular, for the present case of bang-bang control, we will require $p = 1$). Assume further that this reduction mapping

$$\boldsymbol{y} = \boldsymbol{F}(\boldsymbol{q}, \boldsymbol{W}) \tag{109}$$

can be parameterized by constant weights $\boldsymbol{W}$, and that the inverse mapping

$$\boldsymbol{q} = \boldsymbol{G}(\boldsymbol{y}, \boldsymbol{W}) \tag{110}$$

also exists. Then, similar to what done in [20], we can define an error function for the composition of the reduction mapping and of its inverse (also called the auto-associative mapping)

$$S = \left\| \boldsymbol{q}(t) - (\boldsymbol{G} \circ \boldsymbol{F})\,(\boldsymbol{q}(t), \boldsymbol{W}) \right\|^2. \tag{111}$$

For a perfect reconstruction mapping, the sum of error functions evaluated at each point of the trajectory $\boldsymbol{q}(t)$ must be identically zero. In general, this leads to a nonlinear optimization problem, where the matrix of weights $\hat{\boldsymbol{W}}$ represents the optimal solution.

To clarify the meaning of the reduction mapping (109) in a simple case, consider a linear, second-order and non-dissipative mechanical system in free evolution

$$\boldsymbol{M}\ddot{\boldsymbol{q}} + \boldsymbol{K}\boldsymbol{q} = \boldsymbol{0}, \tag{112}$$

where $\boldsymbol{M}, \boldsymbol{K} \in \mathbb{R}^{n \times n}$ are constant, symmetric, and positive definite matrices. Using the eigenvectors $\hat{\boldsymbol{w}}_i \in \mathbb{R}^n$ of the matrix[1] $\boldsymbol{A} := \boldsymbol{K}^{-1/2}\boldsymbol{M}\boldsymbol{K}^{-1/2}$, where $\hat{\boldsymbol{w}}_i$ are normalized so that $\hat{\boldsymbol{w}}_i^T \hat{\boldsymbol{w}}_j = \delta_{ij}$ (the Kronecker delta), the motion of the system (112) can be expressed as

$$\boldsymbol{q}(t) = \hat{\boldsymbol{w}}_1 y_1(t) + \hat{\boldsymbol{w}}_2 y_2(t) + \ldots + \hat{\boldsymbol{w}}_n y_n(t), \tag{113}$$

[1]The matrix $\boldsymbol{A}$ results from the coordinate transformation $\boldsymbol{q} = \boldsymbol{K}^{-1/2}\boldsymbol{z}$, i.e., $\ddot{\boldsymbol{z}} + \boldsymbol{A}\boldsymbol{z} = \boldsymbol{0}$, with $\boldsymbol{A}$ being still symmetric and positive definite. The eigenvectors of $\boldsymbol{A}$ are related to the generalized eigenvectors of $\boldsymbol{K}, \boldsymbol{M}$ [16, chap. 4.5].

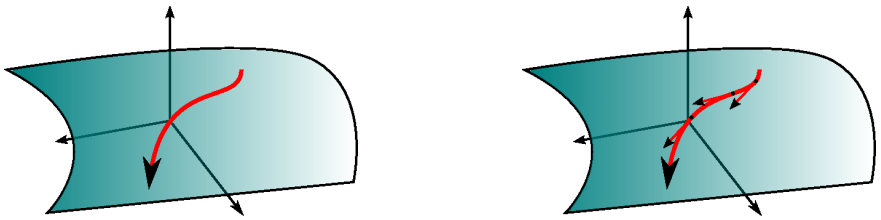

(a) The basic idea of the modal transformation

(b) Local approximation of the modal transformation

Figure 15: Manifold interpretation of modal transformations

where $y_i(t) = \hat{a}_i \sin(\omega_i t - \phi_i)$ are time modulations of the eigenmodes corresponding to motions along $\hat{\boldsymbol{w}}_i$. Hereby, $\hat{a}_i$ are amplitudes, ω_i eigenfrequencies and ϕ_i phase angles. From (113) it can be seen that

$$\boldsymbol{q} = \sum_i \boldsymbol{w}_i y_i, \tag{114}$$

where $\boldsymbol{w}_i \in \mathbb{R}^n$ are parameters of the mappings (114) and $\boldsymbol{q} \in \mathbb{R}^n$ and $y_i \in \mathbb{R}$ represent the instantaneous values of the trajectory $\boldsymbol{q}(t)$ and $y_i(t)$, respectively. Due to orthogonality of $\boldsymbol{w}_i$, the modal reduction mapping has the form

$$y_i = \boldsymbol{w}_i^T \boldsymbol{q}. \tag{115}$$

With the above in mind, we can derive an adaptive law for the linear system (112), so as to learn the true parameters $\boldsymbol{w}_i$ of the mapping (115) under the assumption of unknown (or uncertain) $\boldsymbol{K}$ and $\boldsymbol{M}$. Assume that we measure a new value of the actual joint position $\boldsymbol{q}(k) = \boldsymbol{q}(t_k)$ (with $t_k = kT_s$) at each discrete-time sample k. Consider further the error function

$$S = \frac{1}{4} \left\| \boldsymbol{q}(k) - \sum_i \boldsymbol{w}_i \boldsymbol{w}_i^T \boldsymbol{q}(k) \right\|^2, \tag{116}$$

which represents the squared distance between the input $\boldsymbol{q}(k)$ and the auto-associative mapping $\boldsymbol{w}_i \boldsymbol{w}_i^T \boldsymbol{q}(k)$ obtained composing the reduction mapping (115) and the inverse mapping (114). Then, the gradient descent rule for minimizing S is

$$\tilde{\boldsymbol{w}}_i(k) = \tilde{\boldsymbol{w}}_i(k-1) - \gamma \frac{\partial S(\boldsymbol{q}(k), \boldsymbol{w}_i(k-1))}{\partial \boldsymbol{w}_i}, \tag{117}$$

where $\gamma > 0$ determines the convergence rate and

$$\frac{\partial S(\boldsymbol{q}(k), \boldsymbol{w}_i(k-1))}{\partial \boldsymbol{w}_i} = -y_i(k) \left(\boldsymbol{q}(k) - y_i(k) \boldsymbol{w}_i(k-1) \right). \tag{118}$$

The algorithm (117–118) minimizes the error function (116) recursively, and provides a new guess $\tilde{\boldsymbol{w}}_i \in \mathbb{R}^n$ at each sample k (note that $y_i(k) = \boldsymbol{w}_i^T(k-1)\, \boldsymbol{q}(k)$). However, since the algorithm does not enforce the needed orthonormality of the weights $\tilde{\boldsymbol{w}}_i$, we incorporate in the iteration a Gram-Schmidt orthogonalization (see, e.g., [16, chap. 0.6]) from $\tilde{\boldsymbol{w}}_i(k)$ to $\bar{\boldsymbol{w}}_i(k)$

$$\bar{\boldsymbol{w}}_i(k) = \tilde{\boldsymbol{w}}_i(k) - \sum_{j<i} \boldsymbol{w}_j^T(k-1)\, \tilde{\boldsymbol{w}}_i(k) \boldsymbol{w}_j(k-1).$$

and a successive normalization from $\bar{\boldsymbol{w}}_i(k)$ to the final output $\boldsymbol{w}_i(k)$ at step k

$$\boldsymbol{w}_i(k) = \left(\bar{\boldsymbol{w}}_i^T(k)\,\bar{\boldsymbol{w}}_i(k)\right)^{-1/2}\bar{\boldsymbol{w}}_i(k).$$

Assuming that $\gamma \ll 1$ and neglecting terms of order $O(\gamma^2)$, we obtain the learning rule proposed by [33]:

$$\boldsymbol{w}_i(k) = \boldsymbol{w}_i(k-1) + \gamma\, y_i(k)\Big(\boldsymbol{q}(k) - y_i(k)\boldsymbol{w}_i(k-1) - 2\sum_{j<i} y_j(k)\boldsymbol{w}_j(k-1)\Big). \tag{119}$$

The p dominant eigenvectors $\hat{\boldsymbol{w}}_1, \ldots, \hat{\boldsymbol{w}}_p$ of the data covariance matrix $\boldsymbol{C} = E\{\boldsymbol{Q}\boldsymbol{Q}^T\}$ (of expected values), where $\boldsymbol{Q} = (\boldsymbol{q}(1), \ldots, \boldsymbol{q}(k)) \in \mathbb{R}^{n\times k}$, represent asymptotically stable fixed-points of the difference equation (119) (for a proof, see [32, 39]). For the linear mechanical system (112), the eigenvectors $\hat{\boldsymbol{w}}_1, \ldots, \hat{\boldsymbol{w}}_p$ of the data covariance matrix $\boldsymbol{C}$ are related to the oscillation modes, i.e., $\hat{\boldsymbol{w}}_i$ are eigenvectors of the matrix $\boldsymbol{A}$ that are represented in the particular motion considered. Moreover, in the presence of damping, the eigenvectors of matrix $\boldsymbol{C}$ approximate the eigenvectors of the resonant modes (for more details, see [5]).

To move out of the simple linear mechanical system (112) and consider the full nonlinear dynamics of the links of a multi-dof robot system (either with rigid joints and conventional actuation, or driven by VSA units —the treatment is similar, as shown in Sec. 6.1), the notion of eigenmodes for linear systems might be replaced by so-called nonlinear normal modes [42]. For the present approach, we assume that the dominant mode is synchronous in amplitudes (i.e., the oscillations of the joints are in phase), so that the motion along this mode can be represented by a single curvilinear coordinate. Therefore, when the algorithm described by (119) converges sufficiently fast, the weight vector $\boldsymbol{w}_i(k)$ locally approximates the instantaneous linearization of the nonlinear normal mode. This is sketched in Fig. 15(b). Finally, it is worth mentioning that the order of the weight vectors $\boldsymbol{w}_i(k)$ depend on the particular motion $\boldsymbol{q}(k)$, which the only *information source* of the adaptation algorithm. The first weight vector $\boldsymbol{w}_1$ corresponds to the most dominant principal component of the trajectory $\boldsymbol{q}(k)$, i.e., to the eigenvalue of the matrix $\boldsymbol{C}$ with the largest magnitude.

With the above tools and analysis in mind, assume that we want to excite periodic motions around a reference motor position $\boldsymbol{\theta}_0 \in \mathbb{R}^m$. Consider the PD control

$$\tau = -\boldsymbol{K}_D\dot{\boldsymbol{\theta}} - \boldsymbol{K}_P\left(\boldsymbol{\theta} - \boldsymbol{\theta}_d\right), \tag{120}$$

where $\boldsymbol{K}_D, \boldsymbol{K}_P \in \mathbb{R}^{m\times m}$ are symmetric and positive definite control gain matrices, and $\boldsymbol{\theta}_d \in \mathbb{R}^m$ is the desired motor position for the VSA robot system (9–11), which is taken here as a tunable control input. Then, using $\boldsymbol{w}_1 \in \mathbb{R}^m$ provided by the adaptation algorithm (119), we can compute the following bang-bang control in the direction of the first mode:

$$\Delta\theta_z(\tau_z) = \begin{cases} \text{sign}\,(\tau_z)\,\hat{\theta}_z, & \text{if } |\tau_z| > \epsilon_{\tau_z} \\ 0, & \text{otherwise.} \end{cases} \tag{121}$$

Herein,

$$\tau_z = \boldsymbol{w}_1^T\left(\left(\frac{\partial U_e(\boldsymbol{\theta},\boldsymbol{q})}{\partial\boldsymbol{\theta}}\right)^T - \left(\frac{\partial U_e(\boldsymbol{\theta},\boldsymbol{q})}{\partial\boldsymbol{\theta}}\right)^T\Bigg|_{\boldsymbol{\theta}=\boldsymbol{\theta}_0}\right) \in \mathbb{R} \tag{122}$$

is the generalized force acting in the direction of the first mode, the positive scalar ϵ_{τ_z} is the corresponding threshold, and $\hat{\theta}_z \in \mathbb{R}$ is the modal switching amplitude. Finally, the control input $\boldsymbol{\theta}_d$ in (120) will be adapted as

$$\boldsymbol{\theta}_d = \boldsymbol{\theta}_0 + \Delta\boldsymbol{\theta}. \tag{123}$$

In this way, we can interpret $\Delta\theta_z(\tau_z) \in \mathbb{R}$ as a tangent vector to the modal manifold which transforms with the Jacobian $\boldsymbol{w}_1$ of the inverse reduction mapping (114), i.e., $\Delta\boldsymbol{\theta} = \boldsymbol{w}_1\Delta\theta_z(\tau_z)$.

6.3 Experimental results

The modal decoupling control presented in Sect. 6.1 was tested on the first four VSA joints of the DLR Hand Arm System. The limit cycle controller has been applied either to excite the first or the second mode. Figure 16 shows pairs of plots in the (position/ velocity) phase plane of the modal and joint motion in four different cases. In Fig. 16(a-b), the joint stiffness was preset at the minimum values, while in (c-d) the joint stiffness was increased to half of its maximum feasible value. In both cases, only the first mode motion (blue lines in (a) and (c)) approaches asymptotically the limit cycle, while the remaining modes stay around the origin. In terms of joint motion, the first and the fourth link are those mainly involved (plots blue and magenta in (b) and (d)). In Fig. 16(e), the second mode undergoes cyclic motion (in green) and this involves the motion of all four joints (f). In order to induce all these limit cycle motions, the controlled robot arm was manually pushed from an initial configuration (different for the first and second modes). Finally, the attractive behavior of the limit cycle can be observed in Fig. 16(g) and 16(h), respectively on the modal and joint motion. In this case the robot end-effector has been stopped and then released by hand. After this disturbance, the motion converges back to the limit cycle.

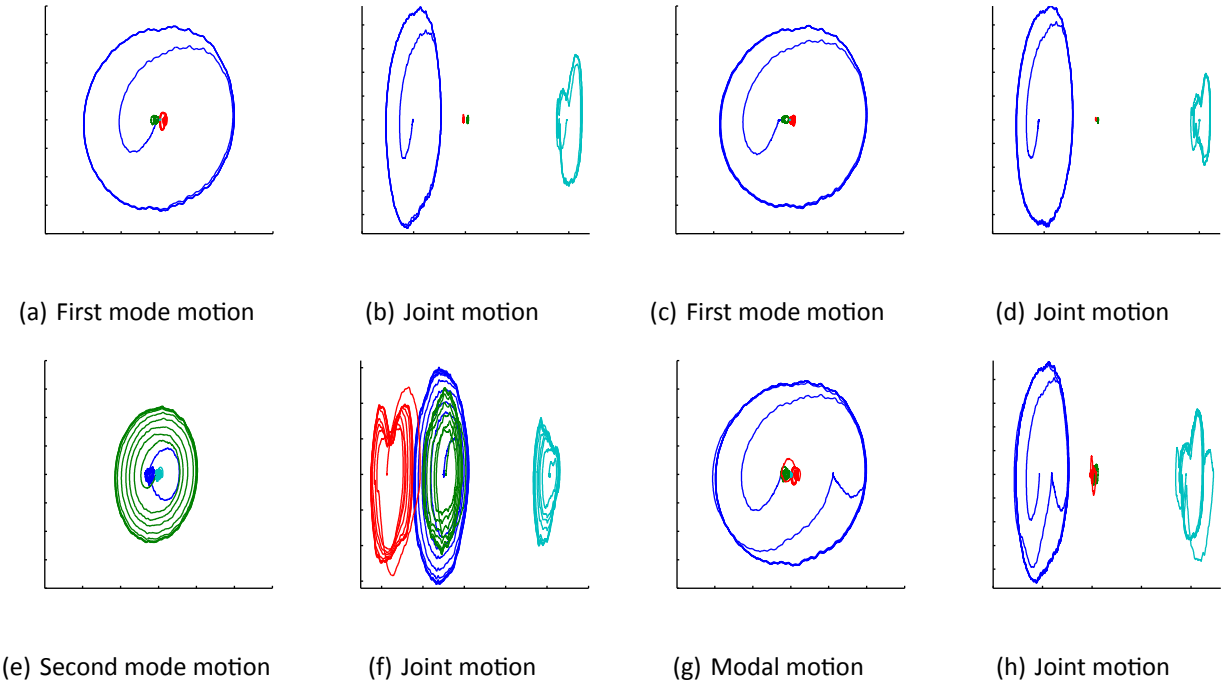

(a) First mode motion (b) Joint motion (c) First mode motion (d) Joint motion

(e) Second mode motion (f) Joint motion (g) Modal motion (h) Joint motion

Figure 16: Phase plots of modal and joint motion in the experimental validation of the modal limit cycle controller for a VSA robotic arm (the first four joints of the DLR Hand Arm System)

The modal adaptive bang-bang control of Sect. 6.2 was tested in a hitting experiment with the DLR Hand Arm System, see Fig. 17(a). As shown in Fig. 17(b), the controller is able to stabilize with this control law a periodic hitting robot motion in the presence of multiple repeated environmental contacts. After the initial disturbance, motion in the y and z directions approaches a periodic steady state within one oscillation cycle.

Finally, to illustrate the adaptability of the control approach, we have performed also some simulations for a robotic system with hybrid dynamics and compliance. For the planar legged robot driven by Serial Elastic Actuators (SEA) shown in Fig. 18(a), an open-loop sinusoidal excitation and the modal adaptive feedback control are compared in Fig. 18(b). In the latter case, the frequency of the vertical oscillation of the trunk converges to the frequency of the task. More simulations are provided in [24].

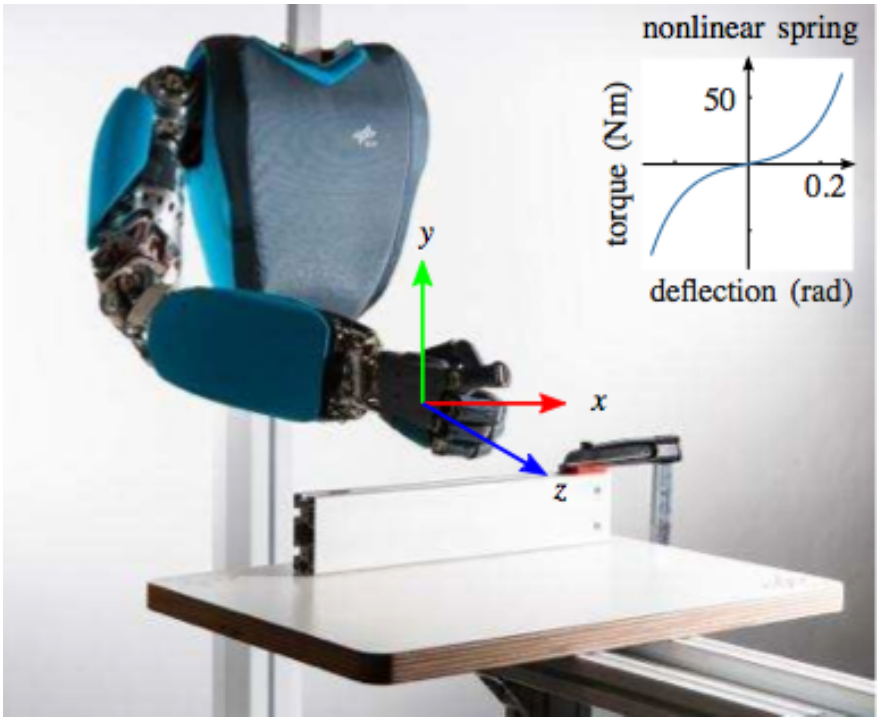

(a) Hardware set-up (with characteristic of the springs in the joints)

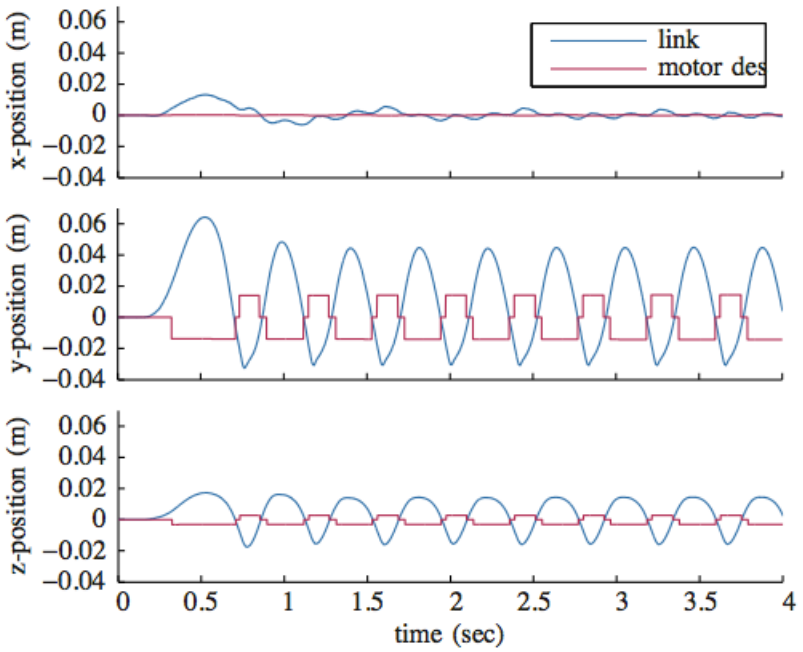

(b) Cartesian motion of the end-effector (in blue) and controlled behavior of the desired motor positions $\boldsymbol{\theta}_d$

Figure 17: Bang-bang modal adaptive control in a hitting experiment with the DLR Hand Arm System

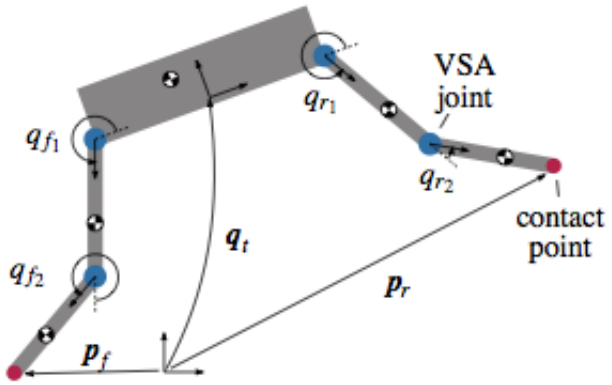

(a) Technical sketch of a planar system with two legs (f = front, r = rear)

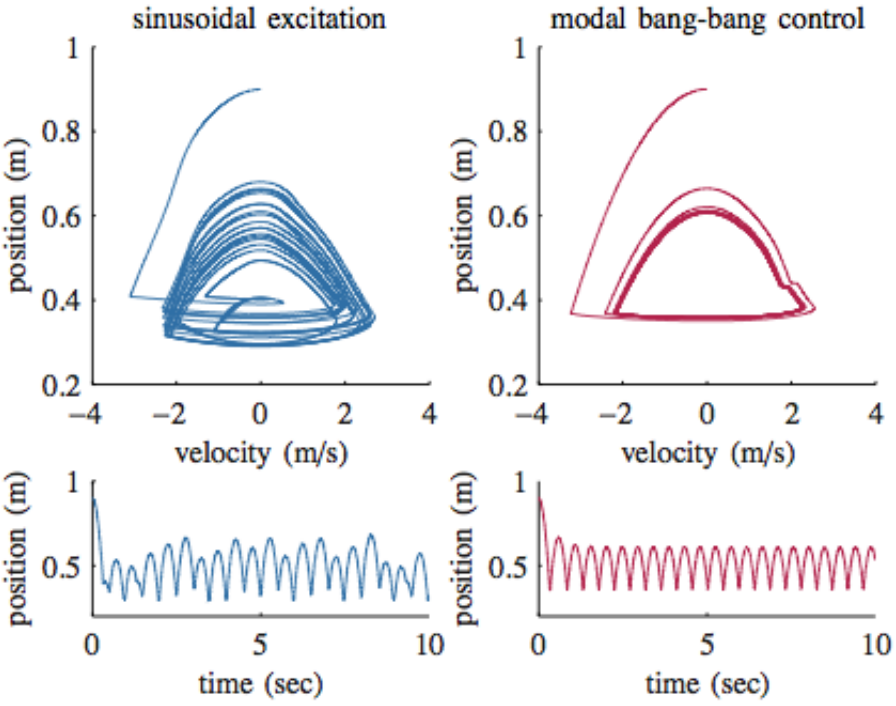

(b) Feedforward sinusoidal excitation (left) and modal adaptive bang-bang control (right) for cyclic hopping motion

Figure 18: Simulation results for a planar legged system with compliant actuation

7 Optimal control for maximizing link velocity of visco-elastic joints

During the first two years of the project, several results have been obtained by the partners on the optimal control of single-dof and multi-dof robot systems, including various form of compliance at the joints (constant elasticity, SEA, VSA, and so on) and considering different objective functions. Early results were summarized already in the form of a milestone (*MS3 Optimal control of modular VSA manipulators*) reached at the end of month 12, while further developments have been presented in scientific papers at conferences and submitted to journals. It is then appropriate to conclude the present document on the control of compliant robots with just one of the latest obtained technical results on this subject.

Two major properties of compliant actuators are the ability to absorb shocks, and to store potential energy in the elastic elements. The latter can be used to realize explosive motions, as those observed in humans [14]. Concentrating on this second advantage of purely elastic joints, we have investigated the role and influence of mechanical damping in visco-elastic joints on the optimal control solution. In particular, we refer to the simple benchmark shown in Fig. 19 . and to the problem of reaching with this 1-dof system the maximum possible link velocity at a given terminal time t_f.

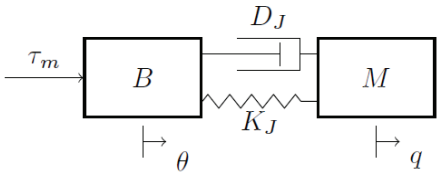

Figure 19: 1-dof visco-elastic Joint

Actuation models of increasing complexity have been considered with the purpose of getting more insight about the influence of a constant joint damping on the optimal control policy for explosive motion tasks. In order to obtain analytical results, we started first by analysing a simple velocity-controlled motor model. The problem of maximizing the link velocity can be formulated mathematically as an Optimal Control problem having just a terminal cost component to mbe minimized (at time t_f)

$$J = -\dot{q}(t_f). \tag{124}$$

A solution to this problem had already been found in the case of undamped elastic joints: The optimal control strategy is bang-bang and periodic with the system's eigenfrequency $\omega = \sqrt{K_J/M}$. By addressing the modified problem for visco-elastic joints we wanted to reveal the effect of damping on the structure of this nominal optimal strategy and to see whether the maximum link velocity would remain bounded by letting t_f go to infinity in the cost functional (124).

Pontryagin's Maximum Principle has been the main mathematical tool used to obtain analytically optimal solutions for simple motor models. On the other hand, for more complex models and cases, we resorted to the numerical optimization software GPOPS. Whenever possible, numerical results were also validated in comparison with analytical results. The theoretical findings show that the optimal control for under-damped joints is again periodic, but is now tuned with the system's damped eigenfrequency $\omega_d = \omega\sqrt{1-D^2}$, where D is the damping ratio. Increasing D leads to an increased period for the optimal control law, but only until the damping ratio is below unity. For critically damped and over-damped joints, the optimal control is no longer periodic and must switch once when a sufficiently large final time is allowed.

Having determined this optimal strategy, we looked at the behavior of the maximum link velocity $\dot{q}_{max}(t_f)$ as t_f increases. While increasing the final time always increases the final achieved link velocity, this increase is bounded and a maximum bound on the link velocity can be found. Figure 20 illustrates the dependence of this bound by plotting the performance index $\epsilon(n, D)$, defined as the ratio of the maximum link velocity $\dot{q}_{max}$ to the maximum motor velocity $\dot{\theta}_{max}$, in terms damping ratios D, as well as for different motor switchings n.

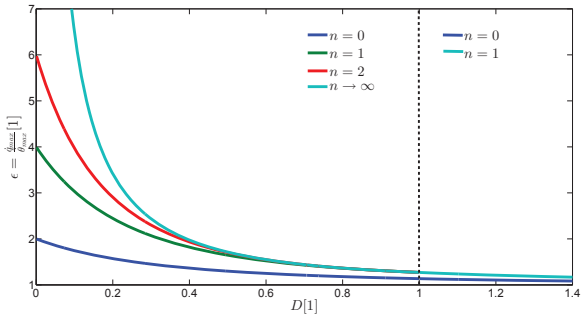

Figure 20: Performance $\epsilon(n, D) = \dot{q}_{max}/\dot{\theta}_{max}$, with input $u_1 = \dot{\theta}$, and $n =$ switchings of u_1^*

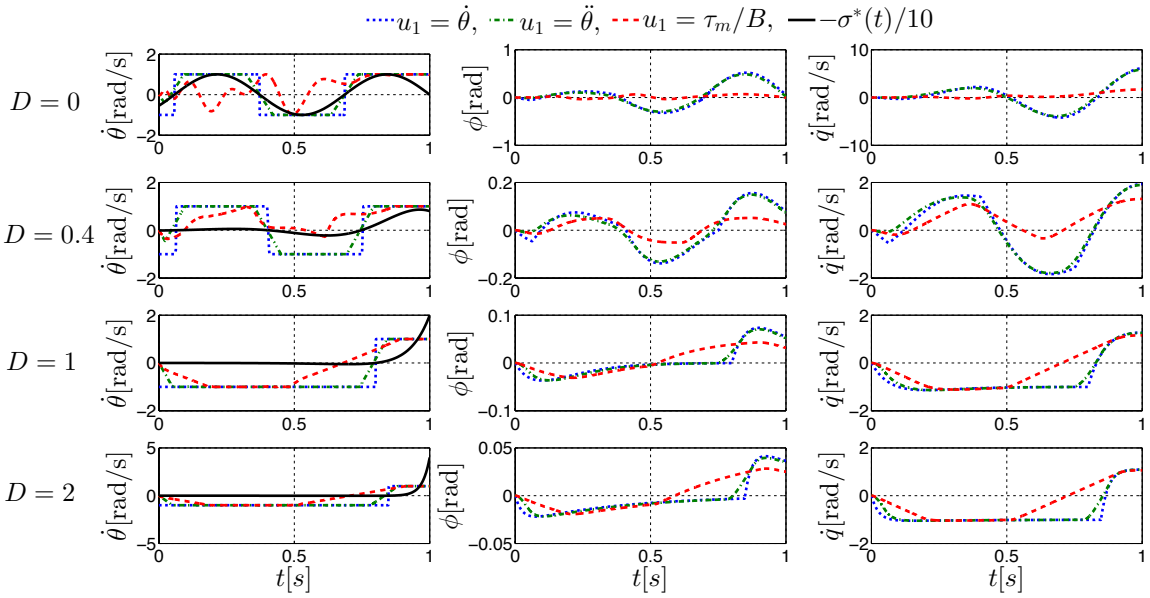

Figure 21: Optimal control results for a visco-elastic joint with different motor models

For the velocity-controlled model, we could also show theoretically that a direct relation exists between the system co-states and the obtained link velocity. This is given by the integral

$$\dot{q}(t_f) = -\int_0^{t_f} \sigma^*(\xi)\,\dot{\theta}(\xi)\,d\xi, \tag{125}$$

where σ^* is the switching function, which is expressed as a linear combination of the system co-states. One advantage of having a valid formula like (125) is the possibility of analyzing the influence of motor velocity on the achieved link velocity along the whole trajectory. Remarkably, the above formula holds for any of the chosen motor models. We can thus interpret the control strategies computed numerically for more complex motor models having acceleration or torque as input by using (125), and in particular the switching function σ^*, see Figure 21. Further analytical and numerical results are contained in the submitted paper [36].

References

[1] A. Albu-Schäffer, O. Eiberger, M. Fuchs, M. Grebenstein, S. Haddadin, Ch. Ott, A. Stemmer, T. Wimböck, S. Wolf, Ch. Borst, and G. Hirzinger. Anthropomorphic soft robotics – From torque control to variable intrinsic compliance. In C. Pradalier, R. Siegwart, and G. Hirzinger, editors, *Robotics Research*, volume 70 of *Springer Tracts in Advanced Robotics*, pages 185–207. Springer, 2011.

[2] A. Bicchi, M. Bavaro, G. Boccadamo, D. De Carli, R. Filippini, G. Grioli, M. Piccigallo, A. Rosi, R. Schiavi, S. Sen, and G. Tonietti. Physical Human-Robot Interaction: Dependability, safety, and performance. In *Proc. 10th Int. Work. on Advanced Motion Control*, pages 9–14, 2008.

[3] S. Bittanti, P. Bolzern, and M. Campi. Recursive least-squares identification algorithms with incomplete excitation: Convergence analysis and application to adaptive control. *IEEE Trans. on Automatic Control*, 35(12):1371–1373, 1990.

[4] R. M. Canetti and M. D. Espa na. Convergence analysis of the least-squares identification algorithm with a variable forgetting factor for time-varying linear systems. *Automatica*, 25(4):609–612, 1989.

[5] B. F. Feeny and R. Kappagantu. On the physical interpretation of proper orthogonal modes in vibrations. *J. of Sound and Vibration*, 4(211):607–616, 1998.

[6] F. Flacco and A. De Luca. Stiffness estimation and nonlinear control of robots with variable stiffness actuation. In *Proc. 18th IFAC World Congr.*, pages 6872–6879, 2011.

[7] F. Flacco, A. De Luca, I. Sardellitti, and N. G. Tsagarakis. Robust estimation of variable stiffness in flexible joints. In *Proc. IEEE/RSJ Int. Conf. on Intelligent Robots and Systems*, pages 4026–4033, 2011.

[8] F. Flacco and A. De Luca. A pure signal-based stiffness estimation for VSA devices. In *2014 IEEE Int. Conf. on Robotics and Automation* (submitted).

[9] F. Flacco, A. De Luca, I. Sardellitti, and N. Tsagarakis. On-line estimation of variable stiffness in flexible robot joints. *Int. J. of Robotics Research*, 31(13):1556–1577, 2012.

[10] G. Garofalo, Ch. Ott, and A. Albu-Schäffer. Orbital stabilization of mechanical systems through semidefinite Lyapunov functions. In *Proc. American Control Conf.*, pages 5715–5721, 2013.

[11] M. Grebenstein, A. Albu-Schäffer, T. Bahls, M. Chalon, O. Eiberger, W. Friedl, R. Gruber, S. Haddadin, U. Hagn, R. Haslinger, H. Höppner, S. Jörg, M. Nickl, A. Nothhelfer, F. Petit, J. Reill, N. Seitz, T. Wimböck, S. Wolf, T. Wüsthoff, and G. Hirzinger. The DLR Hand Arm System. In *Proc. IEEE Int. Conf. on Robotics and Automation*, pages 3175–3182, 2011.

[12] G. Grioli and A. Bicchi. A real-time parametric stiffness observer for VSA devices. In *Proc. IEEE Int. Conf. on Robotics and Automation*, pages 5535–5540, 2011.

[13] S. Gunnarson. On some asymptotic uncertainty bounds in recursive least squares identification. *IEEE Trans. on Automatic Control*, 38(11):1685–1688, 1993.

[14] S. Haddadin, M. C. Özparpucu, and A. Albu-Schäffer. Optimal control for maximizing potential energy in variable stiffness joints. In *Proc. 51th IEEE Conf. on Decision and Control*, pages 1199–1206, 2012.

[15] K. Hoffman and R. Kunze. *Linear Algebra*. Prentice-Hall, 1971.

[16] R.A. Horn and C.R. Johnson. *Matrix Analysis*. Cambridge University Press, 1985.

[17] R. M. Johnstone, C. Richard Johnson, R. R. Bitmead, and B. D. O. Anderson. Exponential convergence of recursive least squares with exponential forgetting factor. *Systems & Control Lett.*, 2(2):77–82, 1982.

[18] M. Kárný, A. Halousková, J. Böhm, R. Kulhavý, and P. Nedoma. Design of linear quadratic adaptive control: Theory and algorithms for practice. *Kybernetika*, 21(7):(1a) 3–96, 1985.

[19] N. Kashiri, M. Laffranchi, J. Lee, N. Tsagarakis, L. Chen, and D. G. Caldwell. A non-invasive real-time method for measuring variable stiffness. In *2014 IEEE Int. Conf. on Robotics and Automation* (submitted).

[20] M. Kirby and R. Miranda. Nonlinear reduction of high-dimensional dynamical systems via neural networks. *Physical Review Lett.*, 72(12):1822–1825, 1994.

[21] M. Laffranchi, N. Tsagarakis, and D. G. Caldwell. A compact compliant actuator (CompAct) with variable physical damping. In *Proc. IEEE Int. Conf. on Robotics and Automation*, pages 4644–4650, 2011.

[22] M. Laffranchi, N. Tsagarakis, and D. G. Caldwell. Analysis and development of a semiactive damper for compliant actuation systems. *IEEE/ASME Trans. on Mechatronics*, 12(2):744–753, 2013.

[23] D. Lakatos, G. Garofalo, F. Petit, Ch. Ott, and A. Albu-Schäffer. Modal limit cycle control for variable stiffness actuated robots. In *Proc.. IEEE Int. Conf. on Robotics and Automation*, pages 4934–4941, 2013.

[24] D. Lakatos, M. Görner, F. Petit, A. Dietrich, and A. Albu-Schäffer. A modally adaptive control for multi-contact cyclic motions in compliantly actuated robotic systems. In *Proc. IEEE/RSJ Int. Conf. on Intelligent Robots and Systems*, pages 5388–5395, 2013.

[25] D. Lakatos, F. Petit, and A. Albu-Schäffer. Nonlinear oscillations for cyclic movements in variable impedance actuated robotic arms. In *Proc. IEEE Int. Conf. on Robotics and Automation*, pages 508–515, 2013.

[26] D.-Y. Liu, O. Gibaru, and W. Perruquetti. Error analysis of a class of derivative estimators for noisy signals. *Numerical Algorithms*, 58(1):53–83, 2011.

[27] L. Ljung. *System Identification: Theory for the User*. Prentice Hall, 1987.

[28] J. G. McWhirter. Recursive least-squares minimization using a systolic array. In *Proc. of SPIE, Real Time Signal Processing V*, pages 105–112, 1983.

[29] T. Ménard, G. Grioli, and A. Bicchi. A real time observer for an agonist-antagonist variable stiffness actuator. In *Proc. IEEE Int. Conf. on Robotics and Automation*, pages 2165–2170, 2013.

[30] T. Ménard, G. Grioli, and A. Bicchi. A stiffness estimator for AA-VSA devices. *IEEE Trans. on Robotics* (submitted), 2014.

[31] S.A. Migliore, E.A. Brown, and S.P. DeWeerth. Biologically inspired joint stiffness control. In *Proc. IEEE Int. Conf. on Robotics and Automation*, pages 4508–4513, 2005.

[32] E. Oja. *Subspace methods of pattern recognition*. Research Studies Press, 1983.

[33] E. Oja. Principal components, minor components, and linear neural networks. *Neural Networks*, 5(6):927–935, 1992.

[34] C. Ott, A. Albu-Schäffer, A. Kugi, and G. Hirzinger. Decoupling based Cartesian impedance control of flexible joint robots. In *Proc. IEEE Int. Conf. on Robotics and Automation*, pages 3101–3107, 2003.

[35] Ch. Ott. *Cartesian Impedance Control of Redundant and Flexible-Joint Robots*. Springer, 2008.

[36] M. C. Özparpucu and S. Haddadin. Optimal control for maximizing link velocity of visco-elastic joints. In *Proc. IEEE/RSJ Int. Conf. on Intelligent Robots and Systems*, pages 3035–3042, 2013.

[37] H. A. Preising and D. W. T. Rippin. Theory and application of the modulating function method–i. Review and theory of the method of the spline-type modulating functions. *Computers and Chemical Engineering*, 17(1):1–16, 1993.

[38] D. J. Sandoz and B. H. Swanick. A recursive least-squares approach to the on-line adaptive control problem. *Int. J. of Control*, 16(2):243–260, 1972.

[39] T. D. Sanger. Optimal unsupervised learning in a single-layer linear feedforward neural network. *Neural Networks*, 2(6):459–473, 1989.

[40] A. Savitzky and M. J. E. Golay. Smoothing and differentiation of data by simplified least squares procedures. *Analytical Chemistry*, 36(8):1627–1639, 1964.

[41] R. Schiavi, G. Grioli, S. Sen, and A. Bicchi. VSA-II: A novel prototype of variable stiffness actuator for safe and performing robots interacting with humans. In *Proc. IEEE Int. Conf. on Robotics and Automation*, pages 2171–2176, 2008.

[42] S. W. Shaw and C. Pierre. Normal modes for non-linear vibratory systems. *J. of Sound and Vibration*, 164(1):85–124, 1993.

[43] J.-J. E. Slotine and W. Li. *Applied Nonlinear Control*. Prentice-Hall, 1991.

[44] M. W. Spong. Modeling and control of elastic joint robots. *ASME J. of Dynamic Systems, Measurement, and Control*, 109(4):310–319, 1987.

[45] J. Vaèko and D. Kocur. Fast tracking RLS adaptation algorithms of the second-order Volterra digital filters. *Radioengineering*, 4(1), 1995.

[46] S. Wolf and G. Hirzinger. A new variable stiffness design: Matching requirements of the next robot generation. In *Proc. IEEE Int. Conf. on Robotics and Automation*, pages 1741–1746, 2008.